

Probing the Electronic Structure of Bulk Water at the Molecular Lengthscale with Angle-Resolved Photoelectron Spectroscopy

Samer Gozem^{a,†}, Robert Seidel^{b,c,†}, Uwe Hergenhahn^{d,e,‡}, Evgeny Lugovoy^{d,f},
Bernd Abel^{d,f}, Bernd Winter^e, Anna I. Krylov^{g,h,*}, Stephen E. Bradforth^{g,*}

^a Department of Chemistry, Georgia State University, Atlanta, GA 30303, USA

^b Helmholtz-Zentrum Berlin für Materialien und Energie,
Albert-Einstein-Straße 15, 12489 Berlin, Germany

^c Humboldt-Universität zu Berlin, Department of Chemistry,
Brook-Taylor-Strasse 2, D-12489 Berlin, Germany,

^d Leibniz Institute of Surface Engineering (IOM), Chemistry Department,
Permoserstr. 15, 04318 Leipzig, Germany

^e Fritz-Haber-Institut der Max-Planck-Gesellschaft, Faradayweg 4-6, 14195 Berlin, Germany

^f University of Leipzig, Wilhelm-Ostwald-Institute for Physical and Theoretical Chemistry,
Linnéstr. 3, 04318 Leipzig, Germany

^g Department of Chemistry, University of Southern California, Los Angeles, CA 90089, USA

^h The Hamburg Centre for Ultrafast Imaging, Luruper Chaussee 149, 22671 Hamburg, Germany

[†] Contributed equally

[‡] Present Address: Max-Planck-Institut für Plasmaphysik, Wendelsteinstr. 1, 17491 Greifswald, Germany

May 18, 2020

Abstract

We report a combined experimental and theoretical study of bulk water photoionization. Angular distributions of photoelectrons produced by ionizing the valence band of neat water using X-ray radiation (250-750 eV) show a limited ($<30\%$) decrease in the β anisotropy parameter compared to the gas phase, indicating that the electronic structure of the individual water molecules can be probed. By theoretical modeling using high-level electronic structure methods, we show that in a high-energy regime photoionization of bulk can be described as an incoherent superposition of individual molecules, in contrast to a low-energy regime where photoionization probes delocalized entangled states of molecular aggregates. The two regimes—low energy versus high energy—are defined as limiting cases where the de Broglie wavelength of the photoelectron is either larger or smaller than the intermolecular distance between water molecules, respectively. The comparison of the measured and computed anisotropies reveals that at high kinetic energies the observed reduction in β is mostly due to scattering rather than rehybridization due to solvation.

Understanding how a solvent affects the electronic properties of solutes is of paramount importance for chemistry. Particularly important are the local solvent structure around solvated molecules and the changes in the shapes and energies of solute’s orbitals induced by the interactions with the solvent. Understanding the local structure of water is crucial in the context of solution chemistry, water in confined environments (e.g., biological water), or water on interfaces (e.g., metal surfaces, or electrodes).

Photoelectron spectroscopy (PES) is a powerful tool for probing electronic structure.¹ The kinetic energies of ejected electrons contain the information about their energy levels within the molecules (molecular orbitals), whereas the photoelectron angular distribution (PAD) encodes the information about the shape of the orbital from which they originate.^{2,3} Although X-ray and ultraviolet PES (XPS⁴ and UPS,^{5,6} respectively) were originally developed for gas-phase molecules in high or ultra-high vacuum,⁷ the liquid-microjet technique⁸ and ambient-pressure instruments⁹ have extended PES to the liquid phase, giving rise to an increasing number of XPS and UPS studies of solutions and liquids.¹⁰

Aqueous-phase XPS and UPS experiments can be used to probe how water molecules interact with solutes and with each other. If a solute’s intrinsic electronic structure is only

weakly perturbed by the solvent, one would expect the PAD of the solute to resemble that of the gas-phase species and the difference between the two could then be attributed to the solvent-induced perturbation of the molecular orbitals of the solute and elastic scattering of photoelectrons.^{11,12} In other words, if the solute maintains its chemical identity, as imprinted in the respective molecular orbitals, then the PAD of solvated species should maintain the gas-phase attributes, even if new features or energetic shifts emerge due to hydrogen-bonding or electrostatic interactions. However, what about a neat substance like liquid water? The bulk is likely to have a delocalized valence electronic structure, akin to excitonic bands in molecular solids.¹³ Indeed, electronic-structure calculations of water clusters^{14–16} have shown the delocalization of the valence states over many water molecules, except for valence states at the band edge (i.e., at low or high ionization energy). Of course, the extent of delocalization depends on how ordered the system is as well as the shape and energy of the molecular orbital. For example, valence bands in highly ordered solids show perfect band structure while compact core orbitals remain localized. Should one then expect the PAD of bulk water to be entirely different from the PAD of water vapor due to delocalization? Or would water in bulk maintain some semblance of its individual electronic character? To which extent does thermally induced disorder affect delocalization? For example, in a perfect water crystal at 0 K, degenerate atomic orbitals might form a perfect delocalized band, but local disorder in liquid water would induce localization, meaning that localization is a function of disorder.

In this work, we attempt to answer these questions by measuring the PAD of the valence states of neat water using high-energy electromagnetic radiation (ranging over several hundreds of electron-volts) and computing the anisotropy parameter β from first principles. Although several studies have interrogated these questions by measuring PADs of neat or doped water clusters and microjets,^{11,12,17–21} a complete picture is still elusive. The main challenge stems from many competing effects, such as intrinsic changes in the electronic structure, elastic and inelastic scattering, and surface versus bulk sensitivity that might affect the experimental observables and that are difficult to disentangle theoretically^{22,23} (in this context, elastic scattering for the most part refers to quasi-elastic scattering, i.e., including electrons inelastically scattered by low-energy phonons but still appearing within the same photoelectron peak shape). Moreover, the signatures of these phenomena and the magnitude of the relevant cross sections

are system- and energy-dependent. For example, it is not obvious to what extent changes in the PAD of bulk water compared to the gas phase are due to intrinsic changes in the electronic structure of water molecules (i.e., due to delocalization or changes in orbital shape due to rehybridization and loss of symmetry) or due to scattering.^{12,17–19,21,23,24} The work by Thürmer *et al.*¹⁷ helps to disentangle these two effects by measuring the PAD for ionization of the $1s_O$ core orbital of water. Because this core orbital should not be significantly perturbed by the other water molecules and should, therefore, retain its shape, any difference between the measured PAD in a microjet and the ideal PAD of $\beta=2$ (at high energies) for an isolated water molecule²⁵ (obtained as a theoretical or an experimental gas-phase PAD) can be attributed to scattering from the neighboring waters. Thürmer *et al.* have shown¹⁷ that the anisotropy parameter is reduced by about 20% at photoelectron kinetic energies above 100 eV, reaching the asymptotic value of $\beta \sim 1.6$. The reduction of β was found to be more pronounced at low energies, in agreement with shorter electron attenuation lengths of slow photoelectrons.¹² We note that surface sensitivity of the experiments may affect the interpretation of this result in terms of elastic and inelastic mean free paths.²⁴

These results by Thürmer *et al.* also agree with the observations of Ahmed and co-workers^{26,27} who studied PADs from the $1s$ core orbitals in a variety of nanoparticles. They found that while the β anisotropy parameter is substantially reduced at low kinetic energies, the elastic mean free path increases considerably at high electron energies, resulting in $\beta \approx 2$ expected for ionization of $1s$ orbitals in the absence of scattering.

The results of these earlier studies^{12,17} provide an important stepping stone for the present work: It is reasonable to expect that the extent of scattering should be the same for the ionization of the valence bands of water with a similar electron kinetic energy as for the $1s_O$ core orbital, so any further reduction in the magnitude of β for the valence orbitals beyond that seen for $1s_O$ can be ascribed to the changes of the molecular orbitals upon solvation.

Recently, Signorell and coworkers have investigated valence PADs in water clusters and microjets,^{11,19,21} with the goal to disentangle different phenomena affecting PADs and to determine the convergence of the anisotropy to the bulk limit. They observed that β at low energy rapidly decreases with the cluster size and concluded that essentially bulk-like electronic structure is attained in clusters of 5-6 water molecules. Consistent with their cluster results and

modeling of scattering, their extrapolation to bulk yielded a significantly reduced β .^{19,21} The crucial difference between the present paper and the work of Signorell and co-workers is the energy range — the latter study has employed low-energy radiation giving rise to photoelectrons much below 100 eV. As discussed in this Letter, this difference leads to strikingly different results.

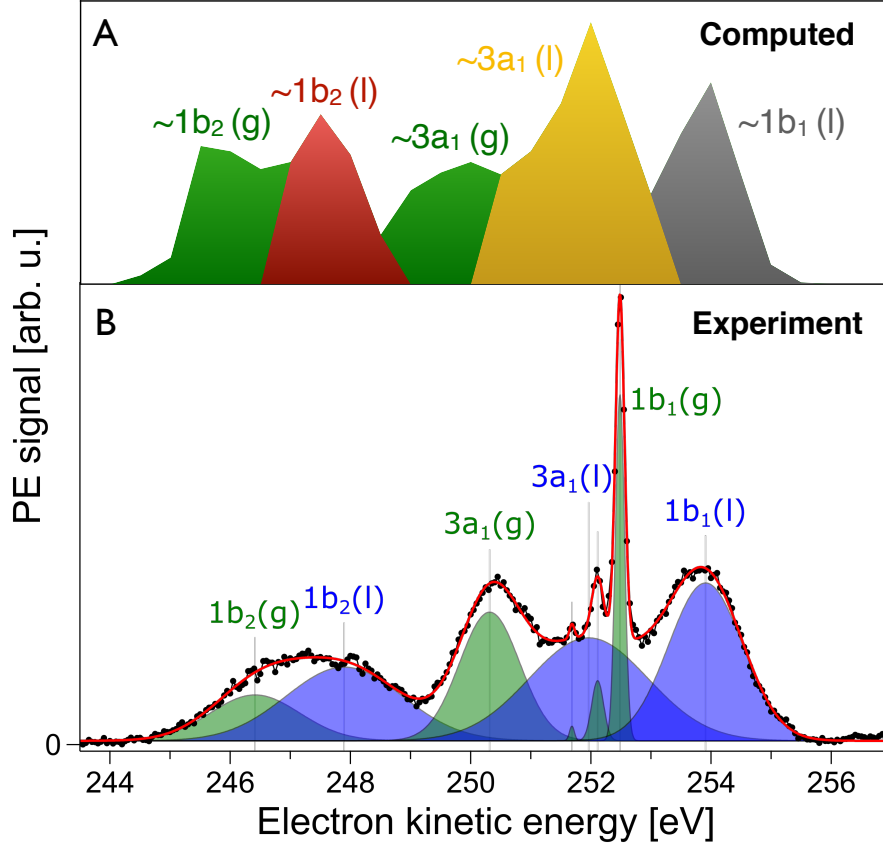


Figure 1: Photoelectron spectrum of liquid water. Top: Theoretical PES computed with EOM-IP-CCSD using pentamer clusters extracted from equilibrium MD simulations of liquid water. The $1b_1$ band (grey) is defined as any state falling in the 9.5-12.5 eV ionization energy range, the $3a_1$ band (yellow) is defined as any state falling in the 12.5-15 eV range, and the $1b_2$ band (red) is defined as any state falling in the 16.5-18.5 eV range. Bottom: Deconvolution fit of the experimental PES (symbols) obtained at $h\nu=265$ eV and $\theta=0$. The fit gives peaks corresponding to ionization from the $1b_1$, $3a_1$, and $1b_2$ orbitals of water for gas phase (green peaks) and liquid (blue peaks).

Fig. 1B shows total valence PES of neat water using a microjet at a photon energy of 265 eV. Fig. S1 in the SI shows an example of the spectrum as a function of θ , which represents the angle between the polarization axis of the incoming light and the orientation of the electron analyzer.

Experimental details of our setups, including the SOL³PES and the LiquidPES station used for the PES measurements at the UE52-SGM beamline at the BESSY II synchrotron radiation facility in Berlin as well as the High Harmonic Generation (HHG) setup at the University of Leipzig, can be found in the SI.

The spectral bands (Fig. 1, and Figs. S1 and S2 in the SI) can be assigned to the ionization from the three highest-energy molecular orbitals of isolated (gas-phase) water molecules and of liquid water. The analysis of the PADs confirms that, as in the core-ionization study,¹⁷ the standard equation (Eq. (S1) in the SI) derived for randomly oriented molecules is valid and that the PAD is determined entirely by the dipole anisotropy parameter β . β values associated with each peak are extracted from fitting the gas-phase features in our spectra. Those β values corresponding to the gas-phase peaks are shown in Fig. 2, along with the wealth of β values from the literature that have electron kinetic energies up to ~ 100 eV.^{28,29} Our HHG result at low photon energy, shown by a green dot in Fig. 2, agrees well with the previous measurements. These HHG β values refine the earlier published values by Faubel *et al.*,³⁰ which were measured in the same HHG lab in Leipzig but lacked a complete set of polarization angles and a proper error analysis. A summary of the experimental data from this work is given in Tables S1, S2, and S3 in the SI.

The PAD of the valence photoelectrons in gas-phase water^{28,29} can be explained by the shapes of the respective molecular orbitals. The $1b_2$, $3a_1$, and $1b_1$ orbitals of water have predominantly p -like character: the $1b_1$ orbital is a pure p -like lone pair orbital whereas $1b_2$ and $3a_1$, which have σ_{OH} character, are slightly distorted by the hybridization and contributions of the $1s_H$ orbitals. Consequently, for all 3 transitions we expect predominantly an s -wave ($\beta=0$) at low electron kinetic energies and the interfering s - and d -waves ($\beta > 1$) at higher energies. This is exactly what is observed here and in the previous experiments,^{28,29} as well as in the calculations using correlated Dyson orbitals and simple photoelectron description (similar trends were reported in an earlier study using density functional theory²⁵). Thus, PADs of gas-phase water clearly show the atomic provenance of the molecular orbitals, while reporting on the variable extent of their hybridization in a molecular environment (e.g., out of the three orbitals, the shape of the $1b_2$ orbital is most deformed, leading to the largest deviations of β from those expected from a pure p -orbital).

The theoretical β s in Fig. 2 were computed using correlated Dyson orbitals, which encode the information about electronic structure before and after the ionization, with the ejected photoelectron wave function treated either as a free particle (plane wave) or as a particle perturbed by the Coulomb potential due to a positive point charge representing the water cation (Coulomb wave). The theoretical framework is described in detail in Refs. 31,32 and in the SI. Although the outgoing electron experiences asymptotically a +1 charge, the Coulomb potential in the vicinity of the target is different due to the screening of the polyatomic nuclear potential by the remaining electrons. The effect of the screening can be accounted for by using effective charges^{31,33,34} and a multi-center expansion.^{33,35-37} Fig. 2 shows the results computed with a plane wave approach ($Z=0$) and with physically motivated effective charges, Z_{eff} computed by Belkić’s rule,³⁴ (Fig. S8 in the SI shows the results with other values of Z_{eff}). In these calculations, we used single-center expansion, with the expansion center placed on the oxygen atom. Belkić’s rule,³⁴ which is based on the generalization of the Rydberg formula for the energy levels of a hydrogen-like atom, yields different Z_{eff} for different bands, because the screening depends on the ionization energy.

In the low-energy regime, where slow outgoing electrons interact with the perturbing molecular potential for a longer time, such a simple treatment of photoelectrons leads to large errors and large differences between the plane wave and Coulomb wave treatments. However, at large energies, fast photoelectrons are less sensitive to the shape of the perturbing cationic potential, such that one can anticipate smaller errors due to the approximate treatment of the free-electron state. Indeed, the difference between the two computational models (using plane waves or Coulomb waves with Z_{eff}) is reduced above kinetic energies of ~ 100 eV. While neither the plane nor the Coulomb wave calculations quantitatively reproduce the experimental data (at high kinetic energies, the theory, on average, overestimates β s for all three bands), the plane wave model reproduces the sharp rise in β at low kinetic energies while the Coulomb wave with Belkić’s charges gives the best agreement at high kinetic energies (mean absolute deviation in β of 0.28, 0.07, and 0.10 for $1b_1$, $3a_1$, and $1b_2$, respectively). This indicates that the simple single-center expansion model employed here captures the variations of the angular distribution of the different ionized states of water using the corresponding Dyson orbitals, which describe deformation of atomic orbitals within a molecular environment. Because the

errors appear to be systematic (theory consistently overestimates β 's), we anticipate that this trend will propagate into the bulk calculations and that the magnitude of the reduction in β could be captured, despite the discrepancy in absolute values. We employ Coulomb waves with Belkić's charges for the rest of the calculations in this work.

How should we modify this simple picture for a water dimer, larger clusters, and eventually bulk? The measurements by Signorell and co-workers^{19,21} on water valence bands suggest that anisotropies in the bulk are quickly washed out, giving rise to strongly reduced β , whereas, as will be presented later in this Letter, our PADs show a persistent anisotropy consistent with a p -like character of the respective Dyson orbitals. To understand these seemingly contradictory findings for bulk water PADs, we start by discussing the theoretical framework for treating photoionization in molecular aggregates (dimers, trimers, etc). Conceptually, should we think about photoionization of the dimer as a sum of two waves coming from each monomer or a single wave corresponding to ionization of an entangled dimer state? Do the coherences between the waves coming from the monomers survive in the bulk or can we treat the dimer photoionization as a sum of two incoherent waves? The answers to these questions determine whether the theoretical model should entail two independent calculations based on localized Dyson orbitals of the monomers or a single-center expansion and a delocalized Dyson orbital of the dimer.

The difference between the two frameworks is illustrated in Fig. 3, which shows β computed for the state derived from the $1b_1$ monomer states of two non-interacting water molecules. For symmetry-identical monomers, the dimer states are two degenerate states corresponding to in-phase and out-of-phase linear combinations of monomer states (essentially, two oxygen's p -orbitals). The PAD computed using each of these delocalized states and a single-center expansion placed in the centroid of the Dyson orbital (that is, in between the two fragments) gives $\beta \sim -0.5$ (red curve in Fig. 3). However, in the case of exactly degenerate states, any linear combination can be used, so instead of the delocalized states one can consider two localized Dyson orbitals as another possible solution. The respective PADs (grey curves in Fig. 3) are monomer-like, giving rise to $\beta \sim 1$. For the two infinitely separated waters, the latter description must be the correct one, but at short distances one may expect the delocalized picture to be more appropriate. The key question is then which model applies better to photoionization of

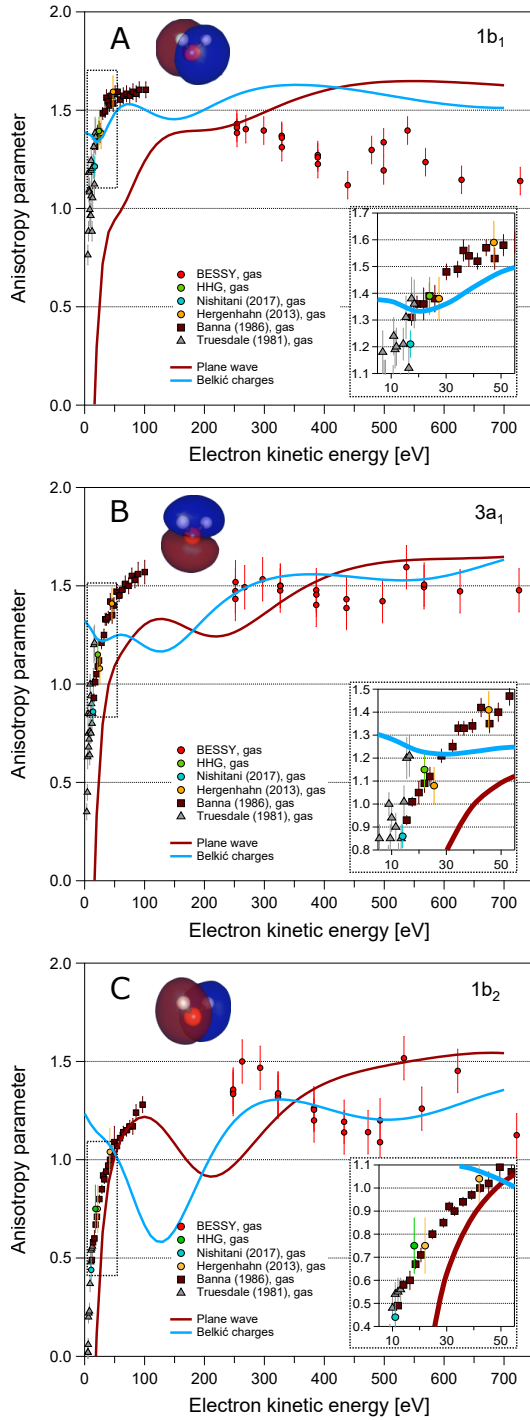


Figure 2: Experimental (symbols) and computed (solid lines) β values for ionization of the $1b_1$ (panel A), $3a_1$ (panel B), and $1b_2$ (panel C) orbitals of vapor-phase water over a range of 700 eV. Experimental data are from Truesdale *et al.*²⁸ (grey triangles), Banna *et al.*²⁹ (brown squares), Nishitani *et al.*²⁰ (cyan circles), Hergenbahn and co-workers¹⁸ (yellow circles), and this work (HHG data in green; BESSY data in red). Computed anisotropies are shown as solid lines using a plane wave (red) and Coulomb wave with Belkić's charges (blue) for the description of the photoelectron. The corresponding EOM-IP-CCSD Dyson orbitals are shown for each transition.

bulk water. Are molecules in the liquid far enough apart to justify a monomer-based treatment of photoionization or should one use delocalized orbitals?

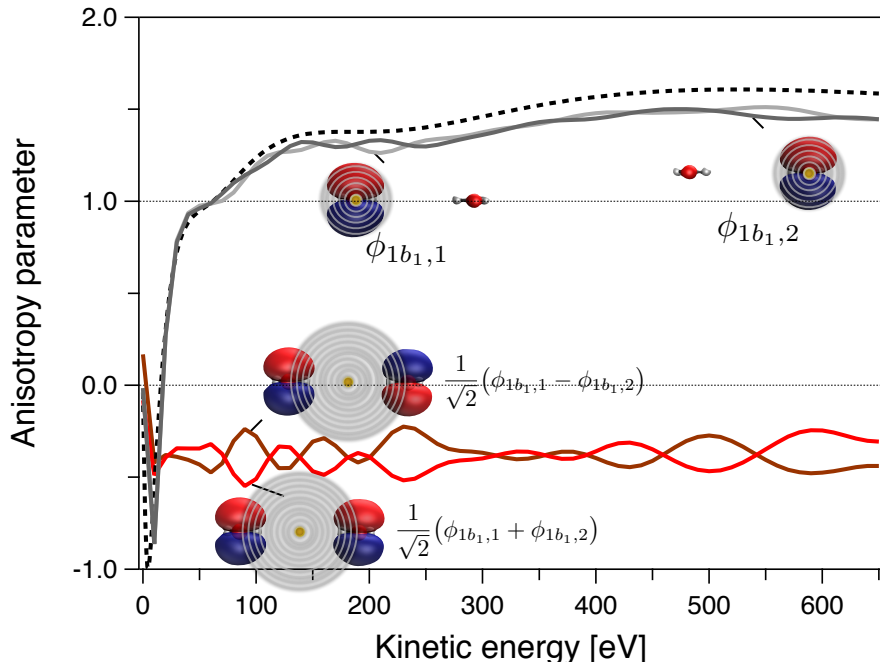


Figure 3: Anisotropies of two non-interacting water molecules computed using localized monomer states (grey) and delocalized dimer states (red). Yellow dots indicate the center of the expansion for the free electron state, which are placed at the centroids of the corresponding Dyson orbitals. The black dashed line shows anisotropies for the $1b_1$ ionized state of the monomer. See text for details.

This exact question has been posed and discussed by Sanov and co-workers³⁸ using photodetachment from dissociating I_2^- , which the authors described as a “molecular interferometer”. They have shown that at large I-I distances, the PAD corresponds to the atomic-like signal (detachment from a p -orbital), whereas at short distances the PAD reflects a delocalized π^* molecular orbital (which has the same symmetry as a d -orbital placed at the middle of the I-I bond). The latter situation can also be described as the interference of the two coherent waves, one coming from each atom. The transition between the two regimes depends on the photoelectron energy, which determines de Broglie wavelength (λ) of the photoelectron: if the distance between the two centers (R) is larger than λ , then one can treat the photodetachment as two independent non-interfering waves, whereas for $\lambda \sim R$ the two waves interfere and the photodetachment signal reveals an entangled state. One can arrive to this intuitive result formally

by analyzing the effect of coherences between the two centers using the multi-center treatment of photoionization^{33,35} (the derivation is given in section II A 1 in the SI). The mathematical reason that the coherences are diminished at high energy is rooted in the oscillatory behavior of the phase between the two waves — the frequency of the oscillations is equal to $\frac{\sqrt{2E}R_{AB}}{2\pi}$, where E is the energy of photoelectrons and R_{AB} is the distance between the two centers. When this frequency is large, the coherences are washed out due to small variations of R_{AB} (due to molecular vibrations or thermal motions in the bulk). However, for small frequencies (when the de Broglie wavelength is shorter than R_{AB}), the coherences between the waves coming off the two centers cannot be neglected. To reconcile this multi-center treatment with a single-center delocalized picture, it is instructive to think about the coherences in the energy domain. At short distances, the energy gap between the two delocalized states of the dimer is large and one can neglect the coherences between the two waves corresponding to photoionization of each state; this justifies the use of a single-center delocalized treatment. However, at large distances, the two delocalized states are degenerate and cannot be treated independently (in other words, the coherences between them cannot be neglected) — this is why the delocalized single-center expansion is physically incorrect when the energy gap between the delocalized states is small relative to the photon bandwidth of the ionizing pulse. Put differently, if the coherences between the photoelectrons produced from the two states are incorporated into the calculations, the correct behavior would be obtained, following the single-center result at low energies and the multi-center result at high energies. Therefore, the magnitude of coherences depends on the representation. In the spatial domain (localized multi-center representation), coherences can be neglected when the two centers are far apart relative to the de Broglie wavelength of the photoelectron. In the energy domain (delocalized single-center expansion), coherences can be neglected when the two centers are close and the energy gap between the delocalized states is large.

Below we discuss the implications of these two distinct regimes in photoionization experiments of bulk water. To simulate the photoionization of bulk water, we consider a model system, a water pentamer cut out from an equilibrium molecular dynamics (MD) simulation of liquid water. To account for thermal motions, we average the results over 100 random snapshots. Our choice of the pentamer is based on the conclusions of a recent study of water

clusters,¹⁹ which suggested that water clusters with five or more waters capture the effect of one solvation shell and, therefore, are a reasonable first-order approximation of bulk water, as far as electronic structure is concerned. In the SI, we present calculations of the anisotropy using the localized approach for larger water clusters, namely $(\text{H}_2\text{O})_6$ and $(\text{H}_2\text{O})_7$, and show that they yield almost identical results to the pentamers.

To model the photoelectron spectra, we compute the EOM-IP-CCSD ionization energies and Dyson orbitals for all valence states for each of the 100 pentamer structures. The computed valence photoelectron spectrum is shown in Fig. 1A. For comparison, Fig. 1B shows a measured valence photoelectron spectrum obtained at 265 eV photon energy and $\theta=0$. The features in the experimental spectrum are broken into the contributions from the liquid and gas-phase water molecules and clearly show distinct bands corresponding to the three valence molecular orbitals of water in each phase. The computed spectrum is obtained as a histogram of the frequency of occurrence of different ionization energies. The computed spectrum also shows the features of both liquid- and gas-phase peaks. Three of the peaks have similar energies and shapes as the experimental spectra of bulk water, and are shown in grey ($1b_1$), yellow ($3a_1$), and red ($1b_2$). Additional peaks (marked by green) in the computed spectrum have energies and shapes that are more similar to the experimental spectra for gas-phase water. These peaks originate from the orbitals localized on surface water molecules, which do not strongly interact with the others and, therefore, resemble gas-phase water more than bulk water. Overall, Fig. 1A illustrates inhomogeneous broadening of 2-4 eV of the individual bands, leading to their partial overlap. A good agreement between the theoretical and experimental spectra provides further support of our computational protocol and justification of using the pentamer model.

To simulate the PAD of bulk water, we computed PADs for each pentamer structure using two different approaches illustrated in Fig. 4. In the first approach, we used delocalized Dyson orbitals and a single-center plane-wave expansion (Fig. 4, top); in this approach, orbital deformation and interference between the immediate neighbors are accounted for, but the coherences between the nearly degenerate electronic states are neglected. In the second approach, we split the Dyson orbital into the fragments contributions, each localized on a single water molecule. We compute the differential cross section for each of the fragment orbitals in the pentamer using a Coulomb-wave expansion with Belkić’s charges centered on the respective fragment, and then

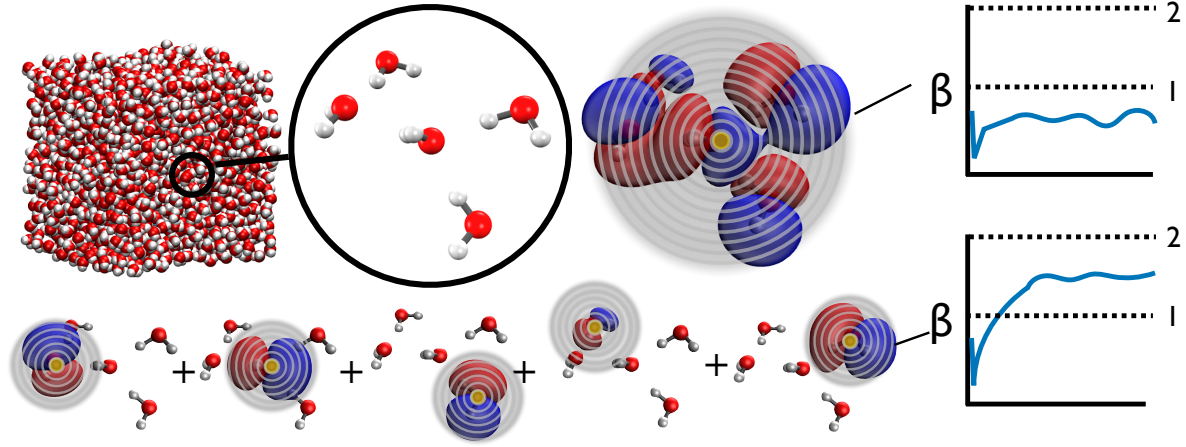


Figure 4: Schematic representation of the two protocols used for our PAD’s calculations. Top left: 100 pentamer geometries were extracted from a molecular dynamics simulation of liquid water. Top center: Representation of the single-center expansion approach, with the center (shown by a yellow dot) placed at the centroid of the delocalized Dyson orbital. This approach yields a more isotropic PAD, as illustrated in the top right drawing. Bottom: Representation of the multi-center approach in which the total PAD is given by the sum of the PADs contributed by each water (yellow dots mark the centroids of the localized Dyson orbitals). These calculations yield anisotropic PADs consistent with the p -like character of the Dyson orbitals, as illustrated by the drawing on the right.

sum up the contributions of the five water molecules to the total PAD (Fig. 4, bottom); in this approach orbital deformation is included, but the interference between neighboring water molecules is neglected. The scattering from nearby waters (or, in other words, the perturbation of the outgoing electron by the potential of the cluster) is neglected in both models.

Fig. 5 shows the computed and experimental β values as a function of kinetic energy for the liquid peaks in the photoelectron spectrum. Also shown are the HHG data from this work (35.6 eV photons) and the data by Nishitani *et al.*²⁰ (29.5 eV photons) for the three valence states of liquid water. The experimental β values are derived by fitting the peak areas for the individual water valence bands (see Fig. 1B, and Tables S1, S2, and S3 in the SI) as a function of the angle between the electron analyzer and the polarization direction. The data shown include four independent runs with 12 different photon energies from the synchrotron and a lower photon energy dataset recorded with HHG radiation. The error bars reflect the fluctuations of the liquid jet position, the fitting errors, and the deviations from the ideal polarization provided by the UE52-SGM-1 beamline. Due to a large peak-overlap and fit constraints, the error bars

for the $3a_1$ and $1b_2$ orbitals are larger than for the $1b_1$ orbital. More details about the data acquisition, data analysis, fitting routine, and the error bar determination is given in the SI.

The experimental β curves reveal considerable similarity between the bulk (Fig. 5) and gas phase (Fig. 2). At high kinetic energies (i.e., above 250 eV), β for bulk ionization ranges around 1-1.25, to be compared with the 1.25-1.5 range for the gas-phase ionization. In both cases, the largest β values are observed for the $3a_1$ band.

The theoretical β values computed using a single delocalized Dyson orbital (dashed line) are strikingly different from those computed by using fragment orbitals and the multi-center expansion (solid lines). The multi-center approach gives β values that are in much better agreement with the experiment for electron kinetic energies above 40 eV, while the single-center expansion model is qualitatively incorrect. To obtain β values corresponding to the $1b_1$, $3a_1$, and $1b_2$ liquid bands theoretically, we select states that fall in the grey, yellow, and red bands of Fig. 1A, respectively. β values computed using the multi-center model systematically overestimate the experimental ones for the liquid, which we attribute to scattering effects not included in the theoretical model.

To understand the implications of the results shown in Fig. 5, let us revisit the analysis of the two limiting regimes of the dimer photoionization (Fig. 3). A qualitatively incorrect β obtained for delocalized Dyson orbitals indicates that in the present experimental regime bulk water ionization can be described as incoherent superposition of the photoionization of individual water molecules rather than photoionization of delocalized entangled states. We can understand this in the context of Sanov and co-worker’s molecular interferometer,³⁸ where the short-time evolution of time-resolved photoelectron images from dissociating I_2^- are discussed in terms of the interference between the two waves coming from the individual atoms. This interference can be described as ionization of a single entangled state spanning both iodine atoms at a short I_2^- bond length. However, at longer times (i.e., at large separations between the atoms) the variation in β ceases and it approaches the asymptotic value corresponding to the PAD of I^- . The distance at which the atoms become independent and the coherences die off is related to the energy of the ionizing radiation, which in turn determines the energy of photoelectrons. In Sanov’s study the distance at which the iodine atoms are no longer coherently ionized (or, said in another way, at which the photoelectrons no longer interfere)

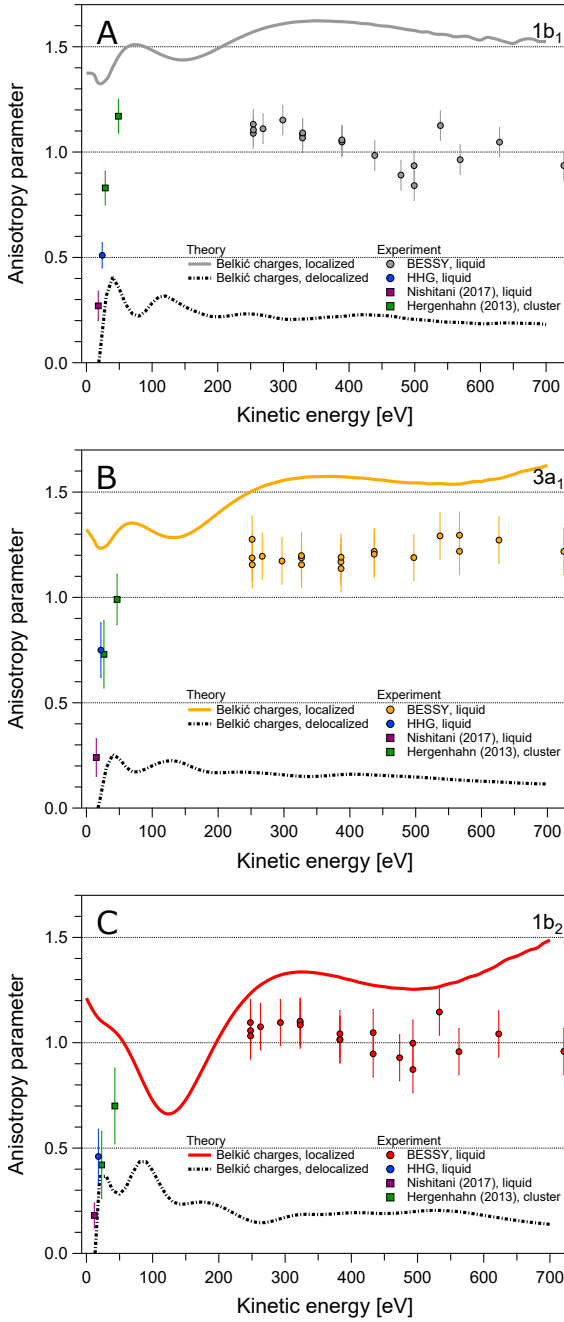


Figure 5: Experimental (symbols) and computed (lines) β values as a function of kinetic energy for valence ionization of liquid water. Grey, yellow, and red denote the values for the $1b_1$, $3a_1$, and $1b_2$ bands. Theoretical β values are assigned based on the energy of the binding energies (see Fig. 1 and associate caption); the delocalized model (dashed lines) shows the result of using a single plane-wave expansion placed at the centroid of the pentamer Dyson orbital, while the localized model (solid lines) computes β by summing the contributions of all valence states of individual waters to the pentamer's PAD. Note that plane waves are used for the delocalized approach, while the localized approach uses physically motivated Belkić's charges (see the SI for details). The experimental fitting procedure is described in the SI. Experimental data are from Nishitani *et al.*²⁰ (liquid microjet, magenta squares), Hergenbahn and co-workers¹⁸ (water cluster, green squares), and this work (HHG indicated by blue circles, BESSY data with circles, color coded depending on the orbital).

was found to be 35 Å, which was in excellent agreement with the de Broglie wavelength of the ejected photoelectrons (0.12 eV).

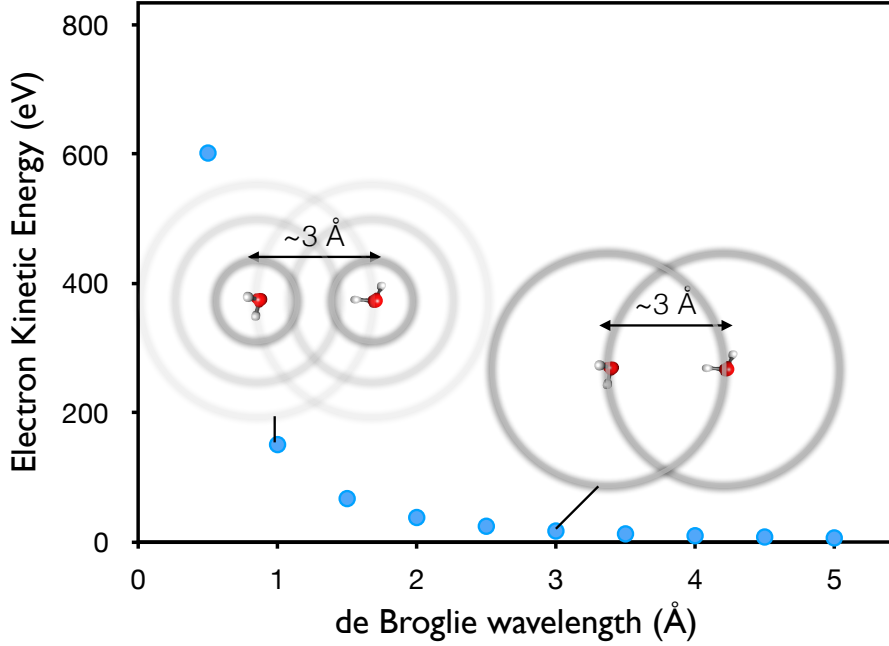


Figure 6: De Broglie relation between the energy of an electron and its wavelength. The distance between two water molecules in the optimized dimer is ~ 3 Å, which corresponds to an electron kinetic energy of ~ 17 eV. At such energies or below, an ejected photoelectron is likely to undergo an interference with the electrons coming off the nearby waters and loses its anisotropy. At higher energies (e.g., at 150 eV, where the electron wavelength is 1 Å) the interference is not significant enough to reduce the photoelectron’s anisotropy.

In bulk water, the typical distance between the centers of two water molecules is on the order of 3 Å. This corresponds to an electron kinetic energy of ~ 17 eV (see Fig. 6). At this energy or lower, the photoionization would likely probe a coherent delocalized state of water (or, using alternative language, reflect the interference between the photoelectrons ejected from the individual fragments). This is consistent with the recent measurements at low kinetic energies by Signorell and co-workers²¹ that show a significant reduction in the β of valence bands from large water clusters. Therefore, at low energies, the single-center expansion of the photoelectron wave function is justified. In contrast, at high energies (e.g., above 150 eV where the photoelectron wavelength is 1 Å), it is more appropriate to describe photoionization using localized orbitals. The observed persistent anisotropy of photoelectrons confirms that water’s valence orbitals retain their identity, despite being slightly distorted (polarized and hybridized)

by their environment. This implies that PES and photoelectron imaging can probe the local electronic structure of a molecule even in a solvent, as long as the ejected photoelectron has a de Broglie wavelength smaller than the proximity of nearby solvent molecules.

To quantitatively analyze the reduction of anisotropies in bulk relative to the gas phase, we consider the reduced β defined as:

$$\beta_{red} \equiv 1 - \frac{\beta_l}{\beta_g}, \quad (1)$$

where β_l and β_g denote liquid and gas-phase anisotropies. If the anisotropy in the liquid phase is the same as in the gas phase, then $\beta_{red} = 0$. Conversely, $\beta_{red} \approx 1$ signifies a complete loss of anisotropy in liquid. The water $1s_O$ core-level study¹⁷ showed that β_{red} decreases as a function of photoelectron kinetic energy and at high kinetic energies (above 200 eV), $\beta_{red} \approx 0.2$. Ahmed and coworkers²⁶ observed a similar trend in β for the $1s_C$ ionization in squalene nanoparticles (at their highest kinetic energy of ~ 40 eV, $\beta \approx 1$, corresponding to $\beta_{red} \approx 0.5$). Interestingly, they observed larger values of β for the $1s_B$ ionization of dry boric acid nanoparticles, approaching 2 at energies above 50 eV.

The reduction of the anisotropy for core ionization at high energies has been attributed by Thürmer *et al.* entirely to elastic scattering, because the shape of the compact $1s_O$ orbital is not perturbed by the interactions with neighboring waters.¹⁷ Our calculations of the anisotropy for $1s_O$ ionization of water pentamers (Fig. S12) yield $\beta = 2$ at electron kinetic energies above 20 eV, thus providing computational support to this conjecture. Our model does not capture the slow rise at low energies (observed both in the gas phase and in bulk), which can be attributed to scattering of photoelectrons from the hydrogens. As evident from the experimental result¹⁷ and from the calculations by Decleva and co-workers for the isolated water molecule,²⁵ the intramolecular scattering becomes irrelevant at ~ 100 eV, considerably below the estimate based on de Broglie equation (164 eV, corresponding to the OH distance).

Fig. 7 shows the experimental and theoretical β_{red} values for core and valence ionization. As in the core-level study,¹⁷ the experimental β values for liquid water show a systematic reduction for valence photoionization. Within the experimental error bars, $\beta_{red} \approx 0.2$ at high energies for both the $1s_O$ and valence orbitals (compare the β values for the data from BESSY in this work with the light-blue curve derived from Thürmer *et al.*). This is surprising because one might expect that the valence orbitals would undergo a further reduction in β upon solvation compared

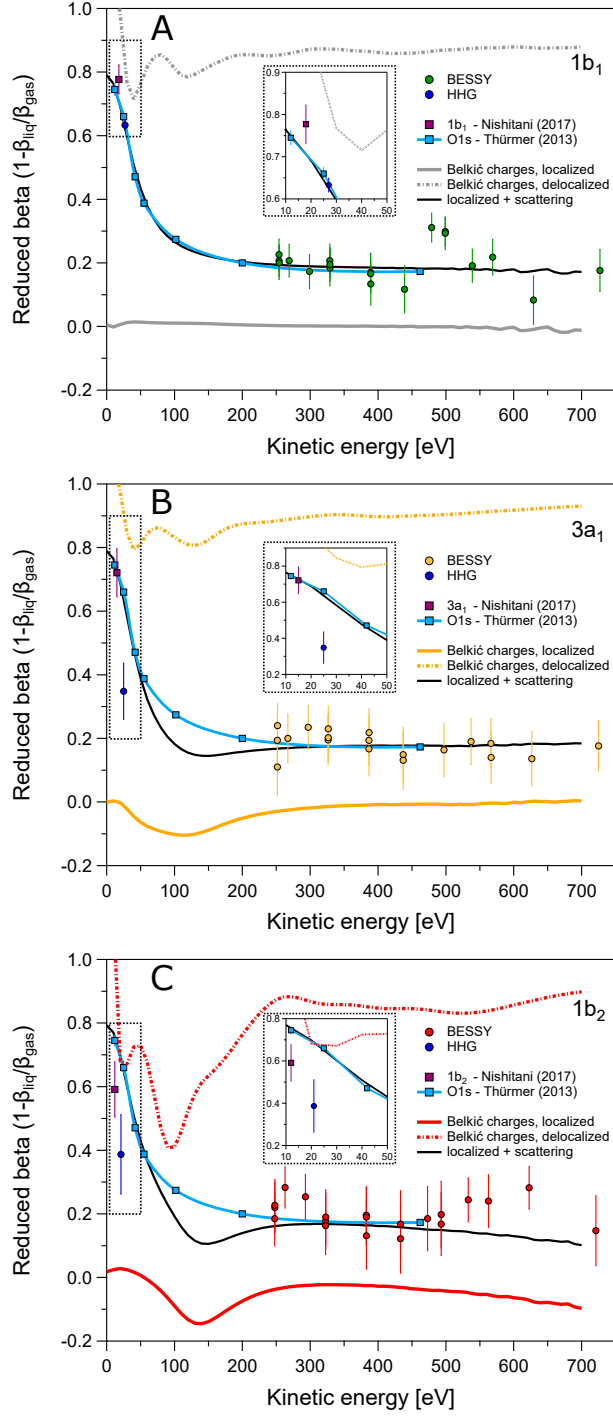


Figure 7: Experimental (symbols) and theoretical (lines) reduced β values for the $1b_1$ (panel A), $3a_1$ (panel B), and $1b_2$ (panel C) bands of water. The blue squares and solid blue line correspond to the reduction in anisotropy due to scattering extracted from the water $1s_O$ core-ionization study.¹⁷ The black lines are the theoretical β values from the multi-center model corrected for the reduction of β due to scattering extracted from the water $1s_O$ experimental data.¹⁷

to the core $1s_O$ orbital due to delocalization or distortion of the orbital shape. However, the theoretical β_{red} from the localized model are zero for all 3 bands, meaning that the interactions with bulk have a rather small effect on the shapes of orbitals of the individual waters, despite significant energetic perturbation, as manifested by the large shifts in the binding energies (by about 1.5 eV, with small variations depending on the orbital shape³⁹) and by inhomogeneous broadening of all 3 valence bands due to solvation (Fig. 1). Thus, despite the participation of the valence orbitals in hydrogen bonding, their shapes remain similar to the shapes of the orbitals in isolated water molecules and the reduction of β at high kinetic energies can be attributed solely to scattering, as in the case of core photoionization.

As expected, the results for the single-center expansion show almost a complete loss of anisotropy ($\beta_{red} \approx 0.8 - 0.9$ at high energies). While this treatment is inappropriate for the high kinetic energy regime, at lower energies it correctly captures the interference effects, which are neglected in the present multi-center treatment. We note that for the lower energy data points from Nishitani *et al.*²⁰ and for the HHG data points, the delocalized model is in excellent agreement with the experiment for all three bands.

To include the effect of scattering in the model, we use the core $1s_O$ data from Thürmer *et al.* Attributing all loss of anisotropy in the $1s_O$ ionization to scattering, we use the ratio of $\beta(1s_O)_g/\beta(1s_O)_l$ (fitted using a sigmoidal function) to scale the theoretical values from the localized model. The resulting curves (shown as dotted lines in Fig. 7) agree very well with the experimental data, confirming our interpretation.

In conclusion, we presented a combined experimental and theoretical study of valence photoionization of liquid water using X-ray radiation. The results show that using sufficiently high energy enables probing the electronic structure of individual water molecules within the bulk. The decrease in anisotropy values in bulk relative to gas-phase water, which can be attributed to the deformation of valence orbitals due to rehybridization, loss of symmetry, and scattering is remarkably small. The high-level *ab initio* calculations show that, despite large energetic perturbation, solvation and hydrogen bonding interactions have a negligible effect on the shape of molecular orbitals. Thus, the reduction of anisotropies can be attributed mostly to scattering. The comparison with the $1s_O$ core-level study further confirms this conclusion.

These results provide an important contribution towards developing a comprehensive pic-

ture of photoionization in the condensed phase and highlight the need for developing a unifying theoretical framework seamlessly connecting low- and high-energy regimes. On the experimental side, more data at intermediate photoelectron energies will help to clarify whether effects of hydrogen bonding and electronic delocalization would be more pronounced at lower energies. To better assess possible effects due to the surface waters and back-scattering of the photoelectrons emanating from gas-phase molecules, experiments with different geometries of the jet (e.g., flat jets) are desirable. Such experiments are currently under way.

Acknowledgments

The authors thank the HZB staff for support during the beamtimes at BESSY II. UH and BW acknowledge funding by the Deutsche Forschungsgemeinschaft (DFG) in the framework of D-A-CH (project SDynG-LI). RS acknowledges an Emmy Noether Young Investigator stipend through the DFG (project SE 2253/3-1). AIK has been supported by the Army Research Office through grant W911NF-16-1-0232. AIK is also a grateful recipient of the 2019 Simons Fellowship in Theoretical Physics and of the Mildred Dresselhaus Guest professorship from the Center for Ultrafast Imaging in Hamburg, which supported her sabbatical stay in Germany. SEB is supported by the U.S. National Science Foundation (CHE-1301465). SG acknowledges the donors of the American Chemical Society Petroleum Research Fund for support through PRF 60837-DNI6.

Supporting information available: Experimental details, computational details, and additional comparisons of gas-phase versus liquid anisotropies. This information is available free of charge via the Internet at <http://pubs.acs.org>.

Conflicts of interest: A.I.K. is the President and a part-owner of Q-Chem, Inc.

References

- [1] Simons, J. In *Photoionization and Photodetachment*; Ng, C.Y., Ed., Vol. 10, Part II of *Advanced Series in Physical Chemistry*; World Scientific Publishing Co., Singapore, 2000.
- [2] Sanov, A.; Mabbs, R. Photoelectron imaging of negative ions *Int. Rev. Phys. Chem.* **2008**, *27*, 53–85.
- [3] Reid, K.L. Photoelectron angular distributions *Annu. Rev. Phys. Chem.* **2003**, *54*, 397–424.
- [4] Nordling, C.; Sokolowski, E.; Siegbahn, K. Precision method for obtaining absolute values of atomic binding energies *Phys. Rev.* **1957**, *105*, 1676.
- [5] Vilesov, F. I.; Kurbatov, B. L.; Terenin, A. N. Electron distribution over energies in photoionization of aromatic amines in gaseous phase *Sov. Phys. JETP* **1961**, *6*, 490.
- [6] Turner, D. W.; Jobory, M. I. Determination of ionization potentials by photoelectron energy measurement *J. Chem. Phys.* **1962**, *37*, 3007.
- [7] Fransson, T.; Harada, Y.; Kosugi, N.; Besley, N. A.; Winter, B.; Rehr, J. J.; Pettersson, L. G. M.; Nilsson, A. X-ray and electron spectroscopy of water *Chem. Rev.* **2016**, *116*, 7551–7569.
- [8] Winter, B.; Faubel, M. Photoemission from liquid aqueous solutions *Chem. Rev.* **2006**, *106*, 1176–1211.
- [9] Salmeron, M.; Schlögl, R. Ambient pressure photoelectron spectroscopy: A new tool for surface science and nanotechnology *Surf. Sci. Rep.* **2008**, *63*, 169–199.
- [10] Seidel, R.; Winter, B.; Bradforth, S. E. Valence electronic structure of aqueous solutions: Insights from photoelectron spectroscopy *Annu. Rev. Phys. Chem.* **2006**, *67*, 283–305.
- [11] Luckhaus, D.; Yamamoto, Y.; Suzuki, T.; Signorell, R. Genuine binding energy of the hydrated electron *Sci. Adv.* **2017**, *3*, e1603224.

- [12] Ottosson, N.; Faubel, M.; Bradforth, S. E.; Jungwirth, P.; Winter, B. Photoelectron spectroscopy of liquid water and aqueous solution: Electron effective attenuation lengths and emission-angle anisotropy *J. Electron Spectrosc. Relat. Phenom.* **2010**, *177*, 60–70.
- [13] Bardeen, C.J. The structure and dynamics of molecular excitons *Annu. Rev. Phys. Chem.* **2014**, *65*, 127–148.
- [14] Pieniazek, P. A.; Sundstrom, E. J.; Bradforth, S. E.; Krylov, A. I. The degree of initial hole localization/delocalization in ionized water clusters *J. Phys. Chem. A* **2009**, *113*, 4423–4429.
- [15] Barth, S.; Ončák, M.; Ulrich, V.; Mucke, M.; Lischke, T.; Slavíček, P.; Hergenbahn, U. Valence ionization of water clusters: From isolated molecules to bulk *J. Phys. Chem. A* **2009**, *113*, 13519–13527.
- [16] doCouto, P. Cabral; Chipman, D. M. Insights into the ultraviolet spectrum of liquid water from model calculations *J. Chem. Phys.* **2010**, *132*, 244307.
- [17] Thürmer, S.; Seidel, R.; Faubel, M.; Eberhardt, W.; Hemminger, J. C.; Bradforth, S. E.; Winter, B. Photoelectron angular distributions from liquid water: Effects of electron scattering *Phys. Rev. Lett.* **2013**, *111*, 173005.
- [18] Zhang, C.; Andersson, T.; Förstel, M.; Mucke, M.; Arion, T.; Tchapyguine, M.; Björneholm, O.; Hergenbahn, U. The photoelectron angular distribution of water clusters *J. Chem. Phys.* **2013**, *138*, 234306.
- [19] Hartweg, S.; Yoder, B. L.; Garcia, G. A.; Nahon, L.; Signorell, R. Size-resolved photoelectron anisotropy of gas phase water clusters and predictions for liquid water *Phys. Rev. Lett.* **2017**, *118*, 103402.
- [20] Nishitani, J.; West, C. W.; Suzuki, T. Angle-resolved photoemission spectroscopy of liquid water at 29.5 eV *Struct. Dyn.* **2017**, *4*, 044014.
- [21] Gartmann, T. E.; Hartweg, S.; Ban, L.; Chasovskikh, E.; Yoder, B. L.; Signorell, R. Electron scattering in large water clusters from photoelectron imaging with high harmonic radiation *Phys. Chem. Chem. Phys.* **2018**, *20*, 16364–16371.

- [22] Jablonski, A.; Powell, C. Relationships between electron inelastic mean free paths, effective attenuation lengths, and mean escape depths *J. of Elec. Spec. and Rel. Phen.* **1999**, *100*, 137–160.
- [23] Michaud, M.; Wen, A.; Sanche, L. Cross sections for low-energy (1-100 eV) electron elastic and inelastic scattering in amorphous ice *Radiat. Res.* **2003**, *159*, 3–22.
- [24] Schild, A.; Peper, M.; Perry, C.; Rattenbacher, D.; Wörner, H. J. Alternative approach for the determination of mean free paths of electron scattering in liquid water based on experimental data *J. Phys. Chem. Lett.* **2020**, *11*, 1128–1134.
- [25] Stener, M.; Fronzoni, G.; Toffoli, D.; Decleva, P. Time dependent density functional photoionization of CH₄, NH₃, H₂O and HF *Chem. Phys. Lett.* **2002**, *282*, 337–351.
- [26] Ahmed, M.; Kostko, O. From atoms to aerosols: probing clusters and nanoparticles with synchrotron based mass spectrometry and X-ray spectroscopy *Phys. Chem. Chem. Phys.* **2020**, *22*, 2713–2737.
- [27] Kostko, O.; Jacobs, M. I.; B. Xu, K. R. Wilson; Ahmed, M. Velocity map imaging of inelastic and elastic low energy electron scattering in organic nanoparticles *J. Chem. Phys.* **2019**, *151*, 184702.
- [28] Truesdale, C.M.; Southworth, S.; Kobrin, P.H.; Lindle, D.W.; Thornton, G.; Shirley, D.A. Photoelectron angular distributions of H₂O *J. Chem. Phys.* **1982**, *76*.
- [29] Banna, M. S.; McQuaide, B. H.; Malutzki, R.; Schmidt, V. The photoelectron spectrum of water in the 30 to 140 eV photon energy range *J. Chem. Phys.* **1986**, *84*.
- [30] Faubel, M.; Siefermann, K. R.; Liu, Y.; Abel, B. Ultrafast soft X-ray photoelectron spectroscopy at liquid water microjets *Acc. Chem. Res.* **2012**, *45*, 120–130.
- [31] Gozem, S.; Gunina, A. O.; Ichino, T.; Osborn, D. L.; Stanton, J. F.; Krylov, A. I. Photoelectron wave function in photoionization: Plane wave or Coulomb wave? *J. Phys. Chem. Lett.* **2015**, *6*, 4532–4540.

- [32] ezDyson user's manual. Gozem, S.; Krylov, A. I. **2015**;
ezDyson, <http://iopenshell.usc.edu/downloads/>.
- [33] Martini, L.; Boll, D. I. R.; Fojón, O. A. Interferences in the photoionization of water molecules *J. Phys. B* **2019**, *52*, 105204.
- [34] Belkić, D. V. z.; Gayet, R.; Salin, A. Electron capture in high-energy ion-atom collisions *Phys. Rep.* **1979**, *56*, 279.
- [35] Ciappina, M. F.; Fojón, O. A.; Rivarola, R. D. Coherent electron emission from simple molecules by impact of energetic charged particles *J. Phys. B* **2014**, *47*, 042001.
- [36] Baltenkov, A. S.; Dolmatov, V. K.; Manson, S. T. Multicentered theory of molecular photoionization *Surf. Rev. Lett.* **2002**, *9*, 1143–1148.
- [37] Baltenkov, A. S.; Manson, S. T.; Msezane, A. Z. Elastic scattering of particle by a system of non-overlapping spherically symmetric potentials *J. Phys. B* **2007**, *40*, 769–777.
- [38] Mabbs, R.; Pichugin, K.; Sanov, A. Dynamic molecular interferometer: probe of inversion symmetry in I_2^- photodissociation *J. Chem. Phys.* **2005**, *123*, 054329.
- [39] Winter, B.; Weber, R.; Widdra, W.; Dittmar, M.; Faubel, M.; Hertel, I. V. Full valence band photoemission from liquid water using EUV synchrotron radiation *J. Phys. Chem. A* **2004**, *108*, 2625–2631.

Probing the Electronic Structure of Bulk Water at the Molecular Lengthscale with Angle-Resolved Photoelectron Spectroscopy:

Supplemental Information

Samer Gozem^{a,†}, Robert Seidel^{b,c,†}, Uwe Hergenhahn^{d,e,‡}, Evgeny Lugovoy^{d,f},
Bernd Abel^{d,f}, Bernd Winter^e, Anna I. Krylov^{g,h,*}, Stephen E. Bradforth^{g,*}

^a Department of Chemistry, Georgia State University, Atlanta, GA 30303, USA

^b Helmholtz-Zentrum Berlin für Materialien und Energie,
Albert-Einstein-Straße 15, 12489 Berlin, Germany

^c Humboldt-Universität zu Berlin, Department of Chemistry,
Brook-Taylor-Strasse 2, D-12489 Berlin, Germany,

^d Leibniz Institute of Surface Engineering (IOM), Chemistry Department,
Permoserstr. 15, 04318 Leipzig, Germany

^e Fritz-Haber-Institut der Max-Planck-Gesellschaft, Faradayweg 4-6, 14195 Berlin, Germany

^f University of Leipzig, Wilhelm-Ostwald-Institute for Physical and Theoretical Chemistry,
Linnéstr. 3, 04318 Leipzig, Germany

^g Department of Chemistry, University of Southern California, Los Angeles, CA 90089, USA

^h The Hamburg Centre for Ultrafast Imaging, Luruper Chaussee 149, 22671 Hamburg, Germany

[†] Contributed equally

[‡] Present Address: Max-Planck-Institut für Plasmaphysik,
Wendelsteinstr. 1, 17491 Greifswald, Germany

Contents

I. Experimental details	3
A. Photoelectron Angular Distributions	3
B. Measured β Parameters for the Valence Photoelectrons from Microjet Experiments	5
C. Synchrotron Radiation	8
D. Data acquisition, synchrotron radiation data	8
E. Data analysis, synchrotron radiation data	9
F. Higher Harmonic Generation	10
G. Data Acquisition, HHG Data	12
H. Data Analysis, HHG Data	13
II. Computational Details and Additional Data	17
A. Theoretical Framework for Calculation of Anisotropies	17
1. Example: Multi-center treatment and coherences in a dimer	20
2. Details of the treatment of the Dyson orbitals and photoelectron wave function	22
B. Details of calculations for monomer, dimer, pentamer, and larger clusters	25
C. Photoionization of the $1s_O$ core orbitals	28
III. Gas-phase versus liquid anisotropies: Theory and experiment	31
IV. References	34
References	34

I. EXPERIMENTAL DETAILS

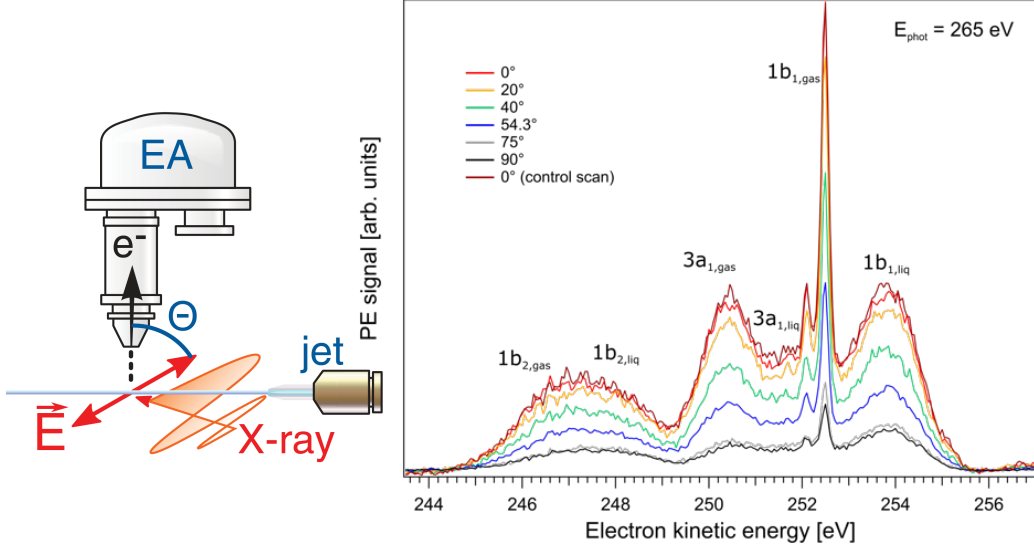


FIG. S1: Photoelectron spectroscopy of liquid water using the microjet technique. Left: Schematic representation of the experimental setup. Water from a liquid microjet is ionized with linearly polarized radiation. The polarization is varied along θ with respect to the orientation of the hemispherical electron analyzer (EA). Reproduced with permission from reference [1]. Right: Photoelectron spectra obtained with 265 eV ionizing radiation at different values of θ . β anisotropy values are derived by fitting the PADs using the cross sections obtained at different values of θ .

A. Photoelectron Angular Distributions

Photoionization with photon energies below 1 keV is well described within the electric dipole approximation for the photon field[2]. For an unoriented sample, the angular distribution function of the photoelectrons is most easily presented in the laboratory frame. Its general form depends on the polarization state of the ionizing radiation, which can be represented by the Stokes parameters S_{1-3} (Ref. 3). For a non-chiral target in a polar coordinate system with z being the propagation direction of the radiation, x along the horizontal, and θ, ϕ denoting the emission direction, we have[4]:

$$I(S, \theta, \phi) = 1 - \frac{\beta}{2} [P_2(\cos \theta) - \frac{3}{2}(S_1 \cos 2\phi + S_2 \sin 2\phi) \sin^2 \theta]. \quad (\text{S1})$$

Here, S_1 refers to the degree of polarization along the horizontal or vertical axis and S_2 refers to linear polarization with a 45° (135°) degree tilt; P_2 denotes the second Legendre poly-

nomial. β is the angular distribution parameter (or anisotropy parameter), which contains the details of the interaction between photon field, initial state and outgoing electron. Here and below I is normalized to 4π when integrated over the unit sphere. To be interpreted as a differential cross section, the functions should be multiplied by $\sigma/4\pi$, with σ denoting the total photoionization cross section for a particular band. Note that the degree of circular polarization S_3 has no influence on the angular distribution.

It is often more convenient to write this equation in a slightly different form,

$$I(S, \theta, \phi) = 1 - \frac{\beta}{2} \left[P_2(\cos \theta) - \frac{3}{2} p \cos 2(\phi - \lambda) \sin^2 \theta \right], \quad (\text{S2})$$

with p denoting the degree of linear polarization along the major axis of the polarization ellipse and λ denoting the tilt of the ellipse to the horizontal:

$$p \equiv (S_1^2 + S_2^2)^{1/2}, \quad (\text{S3})$$

$$\lambda \equiv \arctan(S_2/S_1)/2. \quad (\text{S4})$$

In most experiments, the angular distribution is measured in the dipole plane, i.e., perpendicular to the propagation direction of the photon beam. Eq. (S2) then simplifies to

$$I(S, \pi/2, \phi) = 1 + \frac{\beta}{4} [1 + 3p \cos 2(\phi - \lambda)]. \quad (\text{S5})$$

In this work, we used this form of the angular distribution to analyze the data. For perfect linear polarization ($p = 1, \lambda = 0$), this is equivalent to the better known

$$I(\phi) = 1 + \beta P_2(\cos \phi). \quad (\text{S6})$$

For ionization by linearly polarized radiation, the electron emission pattern typically shows a propensity for emission along the dipole axis, measured by a positive value of the angular distribution parameter β . The exact value of β , however, depends on the details of the initial state and the ionization process. Determining β from $I(\phi)$ involves a comparison of measurements under at least two different emission angles.

B. Measured β Parameters for the Valence Photoelectrons from Microjet Experiments

Tables S1-S3 summarize the measured anisotropies and the respective error bars for each water band. β values at kinetic energies above 248 eV were measured at the synchrotron radiation facility BESSY II with the LIQUIDPES and SOL³PES setups. Data points at low kinetic energy (18 eV - 1b₂, 22 eV - 3a₁, and 24 eV - 1b₁) were derived from High-Harmonic Generation experiments at the IOM Leipzig. The details for the data analysis in each experiment are given in sections E and H.

TABLE S1: Measured β parameters of the 1b₁ band.

E_{kin} , eV	β , gas	β , liquid	β_{red}
24	1.390(60)	0.510(60)	0.633(17)
254	1.426(70)	1.132(70)	0.207(50)
254	1.408(70)	1.089(70)	0.226(49)
254	1.381(70)	1.105(70)	0.200(52)
269	1.400(70)	1.111(70)	0.207(51)
299	1.393(70)	1.152(70)	0.173(54)
329	1.366(70)	1.084(70)	0.207(52)
329	1.308(70)	1.067(70)	0.184(56)
329	1.356(70)	1.091(70)	0.195(53)
389	1.268(70)	1.053(70)	0.170(60)
389	1.256(70)	1.048(70)	0.166(61)
389	1.222(70)	1.058(70)	0.134(66)
439	1.115(70)	0.984(70)	0.117(74)
479	1.294(70)	0.891(70)	0.311(45)
499	1.333(70)	0.935(70)	0.299(45)
499	1.190(70)	0.841(70)	0.293(51)
539	1.393(70)	1.126(70)	0.191(52)
569	1.232(70)	0.964(70)	0.218(56)
629	1.142(70)	1.047(70)	0.083(76)
727	1.136(70)	0.936(70)	0.176(66)

TABLE S2: Measured β parameters of the $3a_1$ band.

E_{kin} , eV	β , gas	β , liquid	β_{red}
22	1.150(130)	0.750(130)	0.348(88)
251	1.433(110)	1.276(110)	0.110(91)
251	1.473(110)	1.188(110)	0.194(77)
251	1.519(110)	1.155(110)	0.240(69)
267	1.493(110)	1.195(110)	0.200(76)
297	1.533(110)	1.173(110)	0.235(69)
327	1.476(110)	1.188(110)	0.195(77)
327	1.501(110)	1.198(110)	0.202(75)
327	1.499(110)	1.155(110)	0.230(71)
387	1.403(110)	1.169(110)	0.167(85)
387	1.478(110)	1.191(110)	0.194(77)
387	1.455(110)	1.137(110)	0.218(75)
437	1.432(110)	1.218(110)	0.149(86)
437	1.387(110)	1.205(110)	0.131(91)
497	1.422(110)	1.189(110)	0.164(84)
537	1.595(110)	1.292(110)	0.190(72)
567	1.493(110)	1.219(110)	0.184(78)
567	1.506(110)	1.295(110)	0.140(83)
627	1.472(110)	1.272(110)	0.136(85)
725	1.477(110)	1.218(110)	0.176(80)

TABLE S3: Measured β parameters of the $1b_2$ band.

E_{kin} , eV	β , gas	β , liquid	β_{red}
18	0.750(130)	0.460(130)	0.387(125)
248	1.346(110)	1.096(110)	0.185(86)
248	1.357(110)	1.058(110)	0.220(80)
248	1.334(110)	1.032(110)	0.227(81)
263	1.500(110)	1.076(110)	0.283(65)
293	1.468(110)	1.096(110)	0.254(70)
323	1.333(110)	1.096(110)	0.177(88)
323	1.319(110)	1.103(110)	0.163(91)
323	1.338(110)	1.084(110)	0.190(86)
383	1.262(110)	1.014(110)	0.196(90)
383	1.200(110)	1.043(110)	0.131(105)
383	1.254(110)	1.015(110)	0.190(91)
433	1.193(110)	1.048(110)	0.122(108)
433	1.139(110)	0.947(110)	0.168(105)
473	1.140(110)	0.929(110)	0.185(101)
493	1.200(110)	0.998(110)	0.168(99)
493	1.089(110)	0.873(110)	0.198(104)
533	1.516(110)	1.146(110)	0.244(69)
563	1.260(110)	0.958(110)	0.240(83)
623	1.452(110)	1.042(110)	0.282(67)
721	1.125(110)	0.959(110)	0.147(110)

C. Synchrotron Radiation

Data for kinetic energies of the photoelectron above ≈ 250 eV were recorded using synchrotron radiation. Experiments were carried out with the LIQUIDPES and with the SOL³PES setups[5] at the UE52/SGM-1 beamline of the BESSY II electron storage ring at Helmholtz-Zentrum Berlin. The relative angle between the analyzer and the polarization axis was varied by rotating the axis of linear polarization of the synchrotron radiation produced in an Apple II undulator[6, 7]. Its design enables generation of linearly polarized radiation with a direction of the polarization vector which is arbitrary within a 90° sector. By virtue of this setup, angular distribution measurements can be carried out without mechanically rotating the electron analyzer. Polarization properties of the so-produced radiation were measured for a single photon energy ($h\nu = 851$ eV)[8]. We observed a systematic decrease of the degree of linear polarization p from 1.0 for horizontal polarization to ≈ 0.965 for vertical polarization, as well as a systematic deviation of the measured direction of the polarization vector from its nominal value, which amounted to $\approx -2^\circ$ for directions between 30° to 80° with the horizontal. We assume that in our experiment the deviations from the ideal polarization are of a similar magnitude.

D. Data acquisition, synchrotron radiation data

We collected synchrotron radiation data in four different beamtimes. In all cases, a liquid jet of water was produced by methods described earlier[9]. Briefly, a liquid water filament with a diameter of $25\ \mu\text{m}$ from a fused silica nozzle was injected into our vacuum chamber. The jet temperature prior injection was held at 10°C by a recirculating chiller (Julabo F12-ED) and the jet velocity was about $40\ \text{m/s}$. A $50\ \text{mM}$ admixture of NaCl was used to prevent sample charging. The energy resolution of the UE52-SGM beamline was better than $70\ \text{meV}$ at $265\ \text{eV}$ photon energy and better than $450\ \text{meV}$ at $1000\ \text{eV}$ photon energy. The exit slit of the beamline was set to a rather large value of $120\ \mu\text{m}$, which lead to a large focal point of similar size, allowing to measure the liquid phase and the surrounding gas sheet of the liquid jet simultaneously. For our experiments, a hemispherical analyzer pointing vertically downward on a horizontal liquid jet was used. While most measurements used the LIQUIDPES setup[9, 10], they were complemented by some data points taken with

the more recent SOL³PES setup[5]. The energy resolution of our hemispherical analyzers was better than 200 meV (SPECS/Leybold, LIQUIDPES) at 20 eV pass energy used, and better than 100 meV (HIP-2 R4000, SOL³PES) at 100 eV pass energy used. No systematic differences between results from the two setups were found, therefore, to reduce clutter, we do not distinguish them in the figures displaying our results in the main text. For a fixed energy, the spectra were recorded starting at vertical linear polarization (0° relative angle between the analyzer and polarization axis), and then going to larger relative angles. The spectra at different angles were recorded over different acquisition times to approximately compensate for the loss of intensity caused by the general shape of the angular distribution function. At the end of the angle series for each energy, a spectrum at 0° relative angle was repeated to check the stability of the liquid jet and the acquisition conditions.

E. Data analysis, synchrotron radiation data

Data were normalized to variation of the current in the storage ring (those were minor, as we recorded most of our data in a continuous injection mode, 'top-up'-operation) and to acquisition time. A Shirley-type background[11–13] was then removed from the spectra. As an initial check of data integrity, the total intensity recorded under each angle was fitted to the angular distribution expression, Eq. (S5). While this leads to a β -parameter the value of which has no particular meaning, excessive deviations of the individual data points from the parameterization are indicative of some problem with the underlying data, *e.g.*, fluctuations of the gas-liquid ratio. Two sets of data (fixed photon energy, multiple angles) were discarded on such grounds. For the remaining, a least squares fit was used to partition the spectrum into contributions from the valence orbitals of water, each with a gas-phase and a liquid-phase component. Typical results are shown in Fig. S2. The water valence band (corresponding to the highest three orbitals, $1b_1$, $3a_1$, and $1b_2$) was fitted by 7 Gaussians, representing the gas-phase and liquid-phase contributions of each orbital. In order to arrive at well-defined results, the following constraints were used for the fit parameters: For the $1b_2(g)$, $1b_2(l)$, $3a_1(g)$, and $1b_1(l)$ values of the peak width (FWHM) were taken from Ref. 14. Additionally, the difference in binding energy between the gas-phase components was set to values from the same work (while their overall position was allowed to vary). Fig. S2 shows that the two components of the $1b_1$ are spectroscopically fairly separated from the

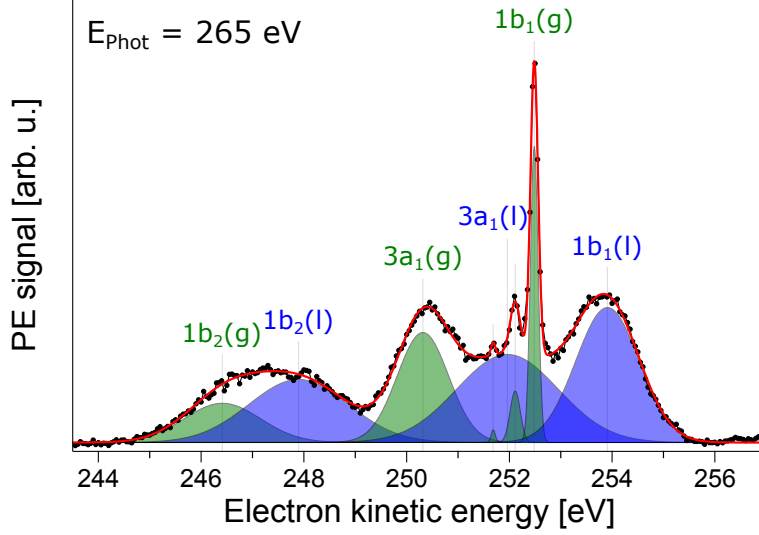


FIG. S2: Decomposition of a measured photoelectron spectrum into gas-phase and liquid contributions pertaining to the three outer valence orbitals. Measured data are shown by symbols, and the result of the fit by a solid line. Labels (g) and (l) denote gas-phase and liquid components.

rest of the spectrum. Therefore, the intensities retrieved for this orbital could, in principle, be determined without peak fitting. In contrast, for the $3a_1$ and $1b_2$ orbitals, the peak areas sensitively depend on details of the fit model.

For each band, the resulting intensities as a function of relative angle between polarization and spectrometer were fitted to Eq. (S5), using σ , β and λ as free parameters (Fig. S3).

Error bars of the β parameter were determined as follows: the observed deviation between the repeated measurements at 0° was interpreted as the impact of uncontrolled fluctuations, *e.g.*, of the liquid jet position, on the experiment. From that a typical relative error of peak area was determined, and was applied to the area under *each* angle. A fit of expression (S5) to the peak areas, taking into account errors as explained above, lead to a resulting error of β of 0.04. We double this error for the orbitals whose peak area depends on details of the fit model ($3a_1$ and $1b_2$). Finally, we linearly add a systematic error of 0.03 to account for deviations from the ideal polarization (as this is an undulator parameter, it might be different for each energy).

F. Higher Harmonic Generation

A data point at low kinetic energy was recorded using a laboratory source for Vacuum-Ultraviolet radiation based on Higher Harmonic Generation (HHG) of a short pulse optical

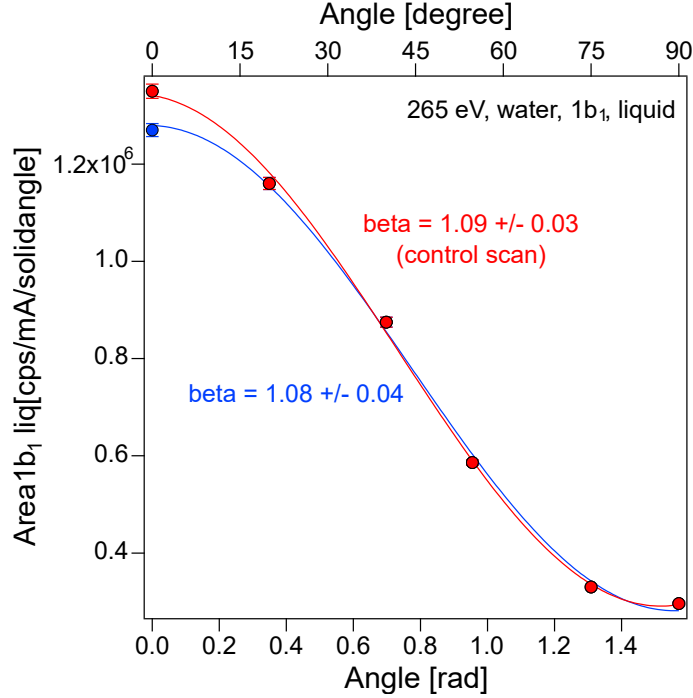


FIG. S3: Area of the first peak in the water valence band as a function of angle between analyzer and polarization direction (symbols). Parameters of the angular distribution function (solid lines) were then determined to best represent the data. As a check of stability of the apparatus, angular distribution fits were carried out taking either the first (blue color) or second measurement at 0° (red color) relative angle. Data points shown in the main text are an average of both values.

laser, using the setup described in Ref. [15]. Briefly, optical radiation from a commercial short-pulse optical laser running at a wavelength of 796 nm is guided into a gas cell filled with Ar for harmonics production. Most experiments used the 23rd harmonics, thus leading to a photon energy of 35.6 eV. In this setup, the direction of polarization was rotated by changing the polarization of the driving laser using a half-wave plate. As the utmost time resolution was not of importance in this experiment, a single higher harmonic was selected by a toroidal grating. A Pt coated 600 l/mm grating with a blaze angle of 1.5° (Yobin Ivon) was used in first diffraction order. Depolarization by reflection on the grating can in principle occur because of different reflectivities for *s*- and *p*-polarized radiation. These effects were estimated using the established simulation program REFLEC[16]. For the conditions encountered in our experiment, tolerable depolarization effects to $\approx p = 0.96$ and angle deviations of $-3^\circ < \lambda < 3^\circ$ from the nominal value were found in the simulation. We summarize these effects in the error bar.

G. Data Acquisition, HHG Data

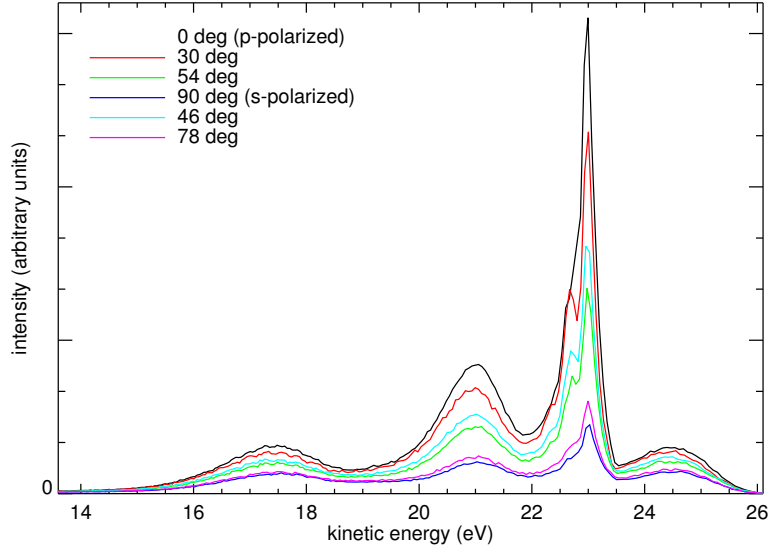


FIG. S4: Electron spectra of a liquid water jet excited by VUV radiation produced in an HHG process. A single harmonic with a photon energy of ≈ 35.6 eV was selected by a diffractive grating. Spectra were normalized to acquisition time and HHG intensity, and are displayed as normalized intensity/energy interval.

The method for producing the liquid jet, and its properties, were very similar to the ones delineated above[15]. Full sets of measurements (six angles each) were repeated on different days, normalized for HHG intensity, and eventually averaged over (‘data 1’). These data were generated using the 23rd harmonic of an 800 nm fundamental, corresponding to a 35.6 eV photon energy. This is the data used in plots in the main manuscript. As an additional cross check, a single set of measurements was carried out at a later stage (and after the set-up has moved into a different laboratory) (‘data 2’). These data were generated using the 25th harmonic of a 796 nm fundamental, corresponding to a 38.9 eV photon energy. A substantial gas-phase contribution is present in all measurements, as the VUV focus is much larger than the liquid jet. Electrons were recorded in a linear time-of-flight analyzer under 90° angle both to the liquid jet (pointing downward in this set-up) and the propagation direction of the radiation. Spectra were converted from time to an energy axis using an empirical relation fitted to gas-phase calibration points. The set of spectra recorded thus is shown in Fig. S4.

H. Data Analysis, HHG Data

We analyzed the angular distribution of the total intensity for the spectra shown in Fig. S4 and for the second set of spectra recorded as a cross-check. Apparent intensity fluctuation showed up in the second data set, attributed to fluctuations of the pump laser. Therefore, this data set is of lower quality, but its analysis is, nevertheless, carried out. On the same occasion, we also recorded a reference data set for molecular water.

Compared to the high kinetic energy spectrum shown in the main text, some differences are apparent in Fig. S4: the gas-phase contribution is more apparent, the HOMO has a relatively lower cross section and in the region between the $3a_1$ and $1b_2$ bands the spectrum is less structured.

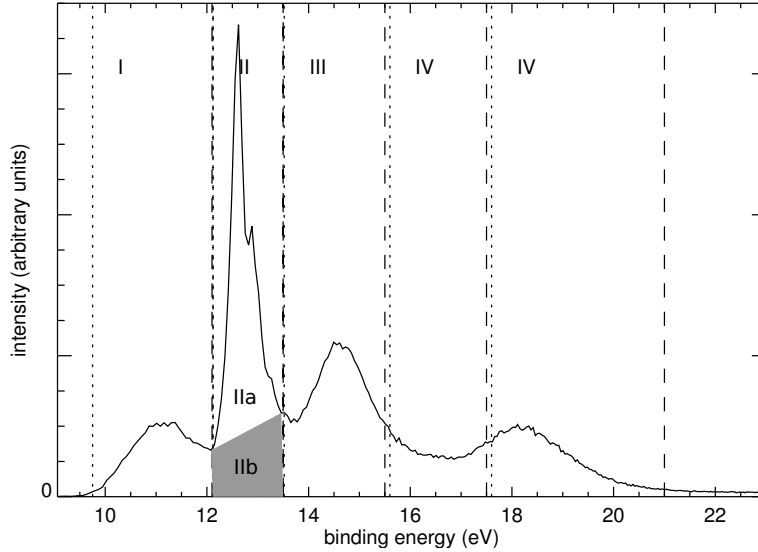


FIG. S5: Regions used to analyze the angular distribution of the water valence spectrum at low kinetic energies.

We carried out the first analysis of angular distribution effects in the spectrum without resorting to least squares fitting. For our gas-phase reference data set, we obtained the values well within the error bar of an earlier study[17]. Next, we separated the gas+liquid spectra in different regions of interest ('roi'), akin to the analysis in Ref. 18 (Fig. S5). The results for β of the different regions are shown in Table S4. We also compare our results for the liquid-jet data to published data for water clusters (size $\langle N \rangle = 58(5)$), recorded with a similar photon energy of 40 eV.

Generally, the results for our liquid-jet experiment are similar to the measurements for

TABLE S4: β parameter for different regions of the valence photoelectron spectrum of liquid water in our HHG experiment and of water clusters[18] recorded with synchrotron radiation of 40 eV photon energy. For liquid water, β was determined either from a fit of intensities at all angles, or from taking into account the spectra at 0° and 90° only. See text for details.

Region	Assignment	cluster ^a	liq liq (0,90) data 1	liq liq (0,90) data 2
I	$1b_1$ (cluster)	0.79(10)	0.50 0.53	0.58 0.55
II ^b	$1b_1$ (mol), $1b_1$, $3a_1$ (cl)	1.21(6)	1.17 1.19	1.06 1.06
IIa	$1b_1$ (mol.)	1.46(8)	1.53 1.61	1.92 2.29
IIb	$1b_1$ (cl.), $3a_1$ (cl.)	0.83(12)	0.80 0.77	0.74 0.61
III	$3a_1$ (mol.), $3a_1$ (cl.)	0.86(10)	0.95 0.97	0.85 0.85
IV	$1b_2$ (mol.), $1b_2$ (cl.)	0.54(10)		
	$1b_2$ (liq.)		0.62 0.63	0.58 0.56
	$1b_2$ (mol.)		0.61 0.63	0.56 0.55
derived				
	$3a_1$ (cl., liq.)	0.73(16)	0.75 0.78	0.73 0.74
	$1b_2$ (cl., liq.)	0.42(16)	0.46 0.49	0.49 0.48

^a Results labeled ‘cluster’ are from Ref. 18.

^b Results in row ‘II’ refer to the sum of rows ‘IIa’ and ‘IIb’.

clusters for all regions of the spectrum, except for the HOMO peak which has significantly lower anisotropy in the liquid case. At least for dataset 1, the results do not vary much if only spectra und 0° and 90° are analyzed, confirming our assumption about a small importance of depolarization effects due to reflection at the grating. Regions IIa and IIb refer to a partitioning of region II into the sharp $1b_1$ gas-phase component and a linear background underlying it, which is assigned to liquid photoemission. For regions III and IV, being a blend of the molecular and liquid $3a_1$ and $1b_2$ orbitals, a β -parameter applying solely to the liquid component can be calculated from the liquid to gas phase intensity ratio and the β -values for the $3a_1$ and $1b_2$ molecular components, measured in separate experiments. Molecular β -values of 1.16 for $3a_1$ and 0.77 for $1b_2$ from our own experiments (see above), in good agreement with literature[17], were used. The liquid to gas-phase ratio was determined from areas of the respective $1b_1$ components measured at an emission angle of 54°, and attributing area I and 50 % of IIb to the liquid $1b_1$. By this procedure, we obtained the values reported in the lowest two columns of Table S4 (labeled ‘derived’).

The results again compare favorably to the values for clusters derived in the same manner. To complement this analysis, we also attempted to derive β -values from a least squares fit. Positions and widths of the gas-phase components were taken from a fit to our reference spectrum, and were only allowed to vary in intensity. To accommodate the more diffuse

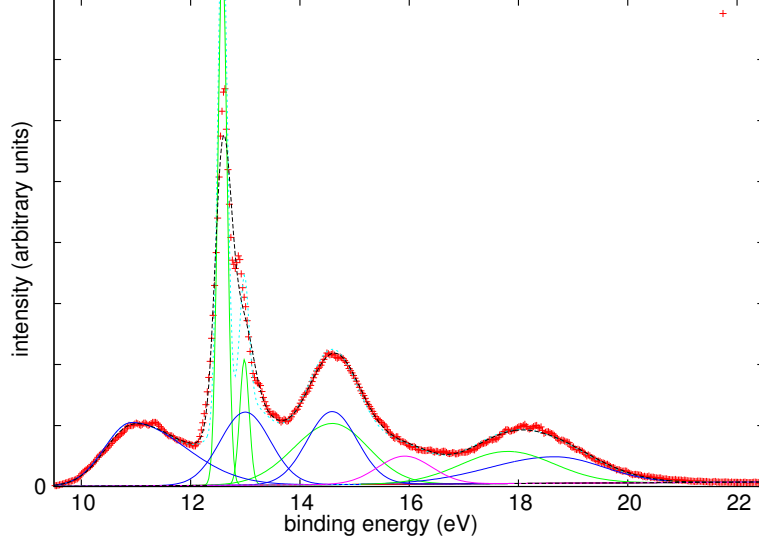


FIG. S6: Decomposition of a photoelectron spectrum measured in the HHG set-up at $h\nu = 35.6$ eV into gas-phase and liquid contributions pertaining to the three outer valence orbitals. Measured data are shown by symbols, and the result of the fit by a broken line. Blue and green color distinguishes peaks assigned to liquid- and gas-phase components, respectively. An auxiliary component, the assignment of which is unclear, is shown in purple color (see text for details). The spectrum measured at the magic angle (54.7°) is shown.

TABLE S5: β -parameter of different regions of the valence photoelectron spectrum of liquid water in our HHG experiment, comparison of fit and roi-analysis. Roi results are repeated from Table S4. Gas-phase values for dataset 2 are given in brackets, as the fit was forced to converge to these via constraints applied to the peak areas under the respective angles (and are taken from Ref. [17]). See text for details.

peak	fit (data 1)	fit (data 2)	roi (data 1)	roi (data 2)
$1b_1(\text{gas})$	1.39	(1.37)	1.53	1.92
$3a_1(\text{gas})$	1.15	(1.16)		
$1b_2(\text{gas})$	0.75	(0.77)		
$1b_1(\text{liq})$	0.51	0.57	0.50	0.58
$3a_1(\text{liq})$	0.88	0.69	0.75	0.73
$1b_2(\text{liq})$	0.49	0.33	0.46	0.49
aux(liq)	0.63	0.84		

nature of the spectra compared to the ones at higher energies we slightly modified the fit model: The liquid $3a_1$ peak was modeled as a doublet with components of equal widths and intensity[14], and we introduced an additional peak (of low intensity) in-between the $3a_1$ and $1b_2$ contributions, which could be assigned to either one of those orbitals. A number of other constraints was applied to the fit parameters of the liquid phase components in order to arrive at well-defined results.

Only spectra at 0° , 54.7° , and 90° were subjected to a least squares fit. Angular anisotropies derived eventually are collected in Table S5, and are compared to the roi-analysis. Deviations are visible, and lead to a slightly higher error bar of the β results for low kinetic energy, compared to the high energy data. As the final result (Tables S1-S3), we quote the values from the roi analysis with the error bars sufficiently large to encompass also the results from areas determination based on peak fitting.

II. COMPUTATIONAL DETAILS AND ADDITIONAL DATA

A. Theoretical Framework for Calculation of Anisotropies

All electronic structure calculations were carried out using *Q-Chem* [19]. Angular distributions were computed with *ezDyson* [20]. The essential elements of the theoretical approach is described in Ref. [21]. Below we provide a brief overview.

PADs and β values are directly related to the differential cross sections. Within certain approximations (see Refs. [20, 22, 23]), the differential cross section can be expressed in terms of a dipole moment element between a Dyson orbital and the photoelectron wave function:

$$\frac{d\sigma}{d\Omega_k} = \frac{4\pi^2 k E}{c} |D_k^{IF}(\theta, \phi)|^2, \quad (\text{S7})$$

$$D_k = \mathbf{u} \langle \Psi_I^N | \mathbf{r} | \Psi_F^{N-1} \Psi_k^{el} \rangle, \quad (\text{S8})$$

where k is the magnitude of the phototelectron wave vector \mathbf{k} , E is the energy of the ionizing radiation, and c is the speed of light. D_k is the photoelectron dipole matrix element. The Dyson orbital, ϕ^d , contains all the necessary information about the molecular system before and after it is ionized,

$$\phi^d(1) = \sqrt{N} \int \Psi_I^N(1, \dots, n) \Psi_F^{N-1}(2, \dots, n) d2 \dots dn, \quad (\text{S9})$$

while the photoelectron wave function Ψ_k^{el} describes the photoelectron. Here we compute Dyson orbitals and ionization energies using an accurate correlated method, equation-of-motion coupled-cluster[24] with single and double excitations (EOM-CCSD).

The current bottleneck limiting the accuracy of the computed cross sections is the photoelectron state, Ψ_k^{el} . The exact treatment would entail solving the Schwinger equation[25] for a giant cluster of water, fully accounting for interactions of the outgoing electron with all other electrons and nuclei. We note that in such fully quantum mechanical treatment there is no “scattering”. What is commonly referred to scattering is the result of the interaction of the outgoing electron with all other electrons and the nuclei. It is an effect of the perturbation of Ψ_k^{el} by the remaining cationic core, which would be completely described by the full quantum-mechanical treatment of the system.

To make this problem tractable, a number of simplifying assumptions are usually invoked. The simplest treatment is to approximate Ψ_k^{el} by a plane-wave (completely neglecting the interaction between the system and ejected electron) or by a Coulomb wave (allowing for a perturbation by a point charge). For anions, this approach combined with a simple plane-wave description of the photoelectron has been shown to reproduce both absolute cross sections and PADs well[23, 26]. Our previous work[21] on absolute cross sections as well as work by others (e.g., Refs. [27]) has also illustrated that Coulomb waves computed with effective charges, accounting for screening effects, can provide a quantitatively accurate description for neutral atoms and (small) molecules.

While in Ref. [21] empirical fitting was used to find optimal charges, Martini *et. al.* used a physically motivated choice based on the generalization of the Rydberg formula for the energy levels of a hydrogen-like atom and referred to as Belkić’s rule[28]:

$$IE = \frac{Z_{eff}^2}{2n^2}, \quad (S10)$$

where IE is the ionization energy and n is the principal quantum number. One can thus evaluate Z_{eff} for different ionized states. In the case of water, using correlated IEs, Z_{eff} equals 1.93, 2.06, and 2.30 for the $1b_1$, $3a_1$, and $1b_2$ orbitals, respectively. For $1s_O$, the effective charge is 6.30, which makes sense because core electrons are not screened by the valence electrons (this value is in perfect agreement with the Slater rule[29]).

It is expected that such simple models would be least accurate in the low-energy regime, where the cross sections are very sensitive to the exact shape of the wave-function (or, said differently, where the outgoing electrons are slow and, therefore, can interact with the perturbing molecular potential for a longer time).

The description of Ψ_k^{el} can be improved by using a multi-center expansion[27, 30] of the delocalized Dyson orbital. A variant of such an approach is described in Ref. [27], where a multi-center treatment was applied to a single water molecule. If executed rigorously, the multi-center model accounts for perturbation of the outgoing electron by a distributed (rather than a single-center) Coulomb potential. If the coherences between the centers are accounted for (as done in Refs. [27, 30]), the multi-center treatment should deliver a more accurate result than a single-center model, both for individual molecules and for clusters. (However, the multi-center expansion does not account for interactions of the

outgoing electron with the electron density of the other centers; hence, it does not include scattering.)

In the multi-center treatment of photoionization, the Dyson orbital is split into the pieces corresponding to the individual centers (i.e., atomic in Ref. [27] and individual water molecules here):

$$\phi^d = \sum_c \phi_c^d \quad (\text{S11})$$

$$\phi_c^d = \sum_{j \in c} a_j \chi_j. \quad (\text{S12})$$

where 'c' denotes individual centers and index j goes over the atomic basis functions (χ_j). Here ϕ_c^d is the piece of Dyson orbital assigned to the center c . Note that ϕ_c^d are not normalized. If the normalized ϕ^d is used, then each ϕ_c^d contributes proportionally to its square norm:

$$||\phi_c^d||^2 = \sum_{j \in c} (a_j)^2. \quad (\text{S13})$$

We assume the orthogonality of ϕ_c^d from different centers (this can be rigorously ensured by standard techniques, such as Löwdin's orthogonalization). Using this expansion, we break the total photoelectron dipole matrix element into the contributions from the individual centers:

$$D_k = \sum_c D_k^c \quad (\text{S14})$$

D_k are complex numbers, so taking its square, as needed for the cross section calculation, includes both incoherent contributions from each center (terms with $c = c'$) and coherences (terms with $c \neq c'$):

$$|D_k|^2 = \left(\sum_c (D_k^c)^* \sum_{c'} D_k^{c'} \right) = \sum_c \sum_{c'} (D_k^c)^* D_k^{c'}. \quad (\text{S15})$$

Each of the individual D_k^c is evaluated using the respective ϕ_c^d and the corresponding Coulomb wave:

$$D_k^c = \langle \phi_c^d(\mathbf{r}) | r_u | \Psi_k^{el}(\mathbf{r} + \mathbf{R}_c) \rangle, \quad (\text{S16})$$

where vector \mathbf{r} is expressed in the coordinate system of the center (local fragment) and vector

\mathbf{R}_c denotes the position of the center c relative to the origin (can be center of charge/mass). Martini and co-workers used an elegant trick, called effective center approximation[27, 30], to simplify the calculation of these cross terms:

$$\langle \phi_c^d(\mathbf{r}) | r_u | \Psi_k^{el}(\mathbf{r} + \mathbf{R}_c) \rangle_r \approx \langle \phi_c^d(\mathbf{r}) | r_u | \Psi_k^{el}(\mathbf{r}) \rangle \times e^{i\mathbf{k}\mathbf{R}_c}. \quad (\text{S17})$$

This means that the contributions from the individual centers come with the phase, which depends on their distance from the origin and the wavevector of the photoelectron (whose magnitude depends on the energy). For the diagonal terms ($c = c'$) this phase cancels out, giving rise to the incoherent contributions. The cross-terms become:

$$(D_k^c)^* D_k^{c'} = \langle \Psi_k | r_u | \phi_c^d \rangle \cdot \langle \phi_{c'}^d | r_u | \Psi_k \rangle \times e^{i\mathbf{k}(\mathbf{R}_{c'} - \mathbf{R}_c)}. \quad (\text{S18})$$

The complete implementation of this approach is beyond the scope of this work. As we demonstrate below, while the coherences are essential in the low-energy part, they are expected to die off when the kinetic energy of photoelectrons exceeds the de Broglie wavelength of the photoelectrons. Experimentally, this was illustrated by Sanov's molecular interferometer[31]. Therefore, in this work we use a simplified approach and compute the photoelectron matrix element Eq. (S8) for photoionization from a water cluster (pentamer) by using the multi-center expansion of the delocalized Dyson orbital and neglecting the coherences. Below, we analyze the effect of coherences for a model emitting dimer.

1. Example: Multi-center treatment and coherences in a dimer

Let us consider ionization from $\phi = \frac{1}{\sqrt{2(1+s_{AB})}}(\chi_A + \chi_B)$ MO in a dimer, such as H_2 , I_2 , or a water dimer. In H_2 , $\chi = 1s$, while in I_2 and the water dimer, it is a p orbital. Here s_{AB} denotes the overlap between the two (normalized) fragment orbitals: $s_{AB} = \langle \chi_A | \chi_B \rangle$.

Using this ϕ as the Dyson orbital, Eq. (S15) becomes:

$$\begin{aligned}
|D_k|^2 &= \frac{1}{2(1+s_{AB})} (\langle \Psi_k | r_u | \chi_A \rangle \langle \chi_A | r_u | \Psi_k \rangle + \langle \Psi_k | r_u | \chi_B \rangle \langle \chi_B | r_u | \Psi_k \rangle) + \\
&\frac{1}{2(1+s_{AB})} \left(\langle \Psi_k | r_u | \chi_A \rangle \langle \chi_B | r_u | \Psi_k \rangle e^{i\mathbf{k}(\mathbf{R}_B - \mathbf{R}_A)} + \langle \Psi_k | r_u | \chi_B \rangle \langle \chi_A | r_u | \Psi_k \rangle e^{i\mathbf{k}(\mathbf{R}_A - \mathbf{R}_B)} \right) = \\
&\frac{1}{2(1+s_{AB})} (\langle \Psi_k | r_u | \chi_A \rangle \langle \chi_A | r_u | \Psi_k \rangle + \langle \Psi_k | r_u | \chi_B \rangle \langle \chi_B | r_u | \Psi_k \rangle) + \\
&\frac{1}{1+s_{AB}} Re \left[\langle \Psi_k | r_u | \chi_A \rangle \langle \chi_B | r_u | \Psi_k \rangle e^{i\mathbf{k}(\mathbf{R}_{BA})} \right], \tag{S19}
\end{aligned}$$

where $\mathbf{R}_{BA} = \mathbf{R}_B - \mathbf{R}_A$. Here the first two terms are contributions from the individual centers and the last term is the coherence between them. Since χ_A and χ_B are identical in our model example, the last term becomes $|\langle \Psi_k | r_u | \chi_A \rangle|^2 \times \cos(\mathbf{k}(\mathbf{R}_{BA}))$. In the united atom limit, $\mathbf{R}_{AB} = 0$, $s_{AB} = 1$, and the total cross section is equal to that of an atom. If we can get rid of coherences at large values of $\mathbf{k}\mathbf{R}_{AB}$, then the cross section becomes again equal to that of one atom, which is the correct result for non-interacting fragments at infinite separation. Likewise, β 's should show consequences of the coherences at small values of $\mathbf{k}\mathbf{R}_{AB}$. Let us analyze this term some more. We note that

$$\mathbf{k}\mathbf{R}_{AB} = \cos(\alpha) \cdot |k| \cdot |R_{AB}|, \tag{S20}$$

where α is the angle between the molecular axis and \mathbf{k} (wave vector of the ejected electron). Now we can look at what happens when we average over the molecular orientations. The integration should be over all values of α (from 0 to π), so $\cos(\alpha)$ changes from one to minus one. The magnitude of $|k| \cdot |R_{AB}|$ term determines the frequency of oscillations of $\cos(\cos(\alpha) \cdot |k| \cdot |R_{AB}|)$. The integration can be expressed in an easier to recognize form:

$$\begin{aligned}
&\int_0^\pi \cos(\cos(\alpha) \cdot |k| \cdot |R_{AB}|) d\alpha = \\
&\int_{-1}^1 \cos(x \cdot |k| \cdot |R_{AB}|) dx = \\
&\int_{-\pi}^\pi \cos(\alpha' \cdot \frac{|k| \cdot |R_{AB}|}{2\pi}) d\alpha' \tag{S21}
\end{aligned}$$

The value of $\frac{|k| \cdot |R_{AB}|}{2\pi}$ gives the number of periods of the integrand spanned by the definite

integral. For integer (and half-integer) values, the integral vanishes. Thus, the coherences are definitely important when $|k| \cdot |R_{AB}| < 2\pi$ or, equivalently, when $\sqrt{2E} \cdot |R_{AB}| < 2\pi$, giving rise to:

$$E < \frac{1}{2} \left(\frac{2\pi}{R_{AB}} \right)^2, \quad (\text{S22})$$

which is identical to the de Broglie equation (in atomic units) connecting the wavelength of the photoelectron with its energy:

$$\lambda = \frac{2\pi}{p} = \frac{2\pi}{k} = \frac{2\pi}{\sqrt{2E}}. \quad (\text{S23})$$

For $R_{AB} \approx 0.9584 \text{ \AA} \approx 1.81$ bohr (OH distance in water molecule), the corresponding energy is 164 eV. For 3 Å (approximately the average distance between water molecules in bulk), we obtain 17 eV (see Fig. 6 in main manuscript). Thus, coherences are expected to be important at energies below these values in the multi-center treatment of water molecules (as in Ref. [27]) and water bulk, respectively. At high energies, however, the coherences die off because of the highly oscillatory nature of the integrand in Eq. (S21). Although for fixed R_{AB} , the oscillations may continue indefinitely, they are washed out when averaging over R_{AB} is carried out because small changes in R_{AB} cause large changes in the value of the integral. This is expected to happen in vibrating molecules and, even more effectively, in bulk, where the distribution of the inter-fragment distances is rather broad: $\sim 0.5 \text{ \AA}$, as eyeballed from the radial distribution function $g(r)$ of water[32].

The analysis of the numerical results in Ref. [27] clearly shows that even without accounting for molecular vibrations, the coherences become rather small above the energies estimated by Eq. (S22)[42].

2. Details of the treatment of the Dyson orbitals and photoelectron wave function

To analyze the implications of different treatments of the Dyson orbital and outgoing electron, we begin by analyzing the PADs for the isolated water molecule.

Fig. S7 shows the effect of the basis set on the computed β using Belkić's charges and single-center expansion. It also compares two different protocols: using Dyson orbital centroid as the center of the expansion for Ψ_k (this is the approach used traditionally, as in Refs. [21, 23]) and using oxygen atom as the expansion center. From these results, we

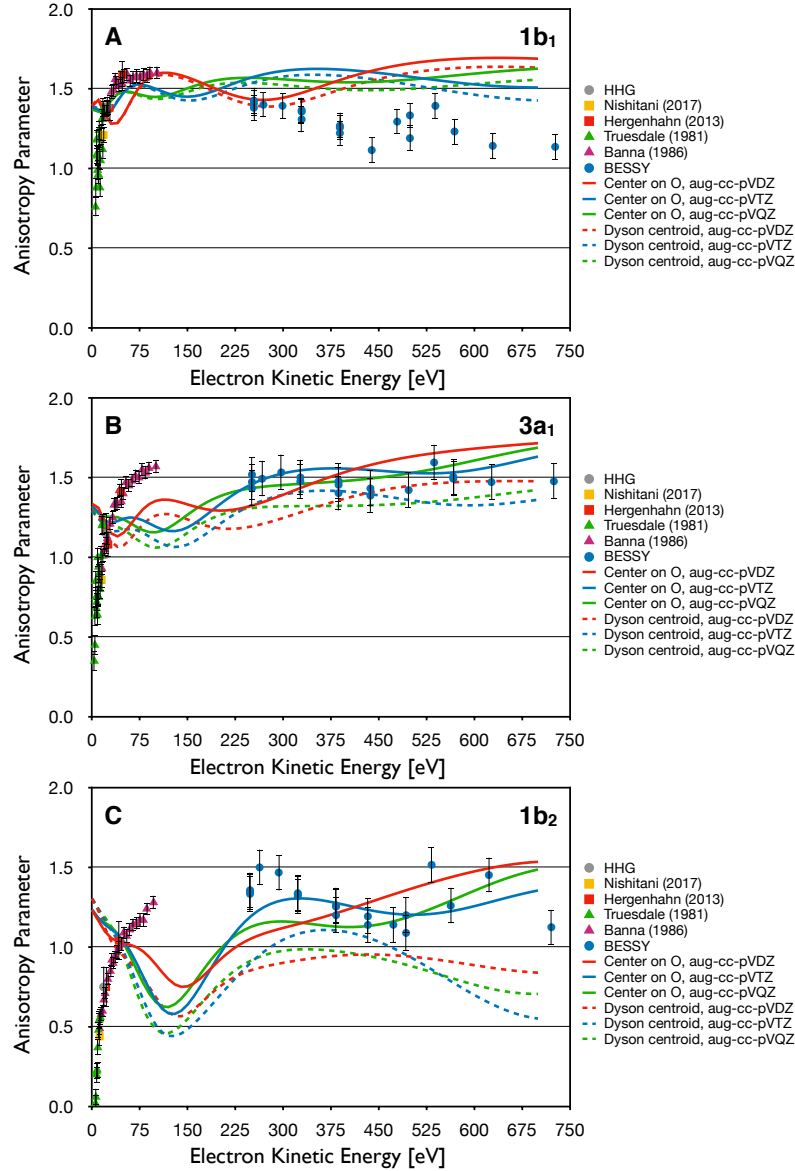


FIG. S7: β for water monomer photoionization computed with different basis sets and Belkić's charges. Results are shown for each of $1b_1$, $3a_1$, and $1b_2$ states (panels A, B, and C, respectively). A single center of expansion is placed at the centroid of the Dyson orbital (dashed) or at the coordinates of the oxygen atom (solid lines).

observe the following:

- Using the centroid of the Dyson orbital as an expansion center for Ψ_k artificially exaggerates the contributions of higher angular momenta. We observe that the center is slightly offset from the oxygen, despite the fact that the Dyson orbital is dominated by the O($2p$) orbital.

- The solid lines (center on oxygen) agree better with the experimental results, especially for $1b_2$ in which the center of the Dyson orbital is further from the oxygen. The mean absolute deviations in β are 0.28, 0.07, and 0.10 for $1b_1$, $3a_1$, and $1b_2$, respectively
- A double- ζ basis is not sufficient: aug-cc-pVTZ agrees better with the experiment. Quadruple- ζ results still show some differences, but they are smaller than the change from aug-cc-pVDZ to aug-cc-pVTZ.

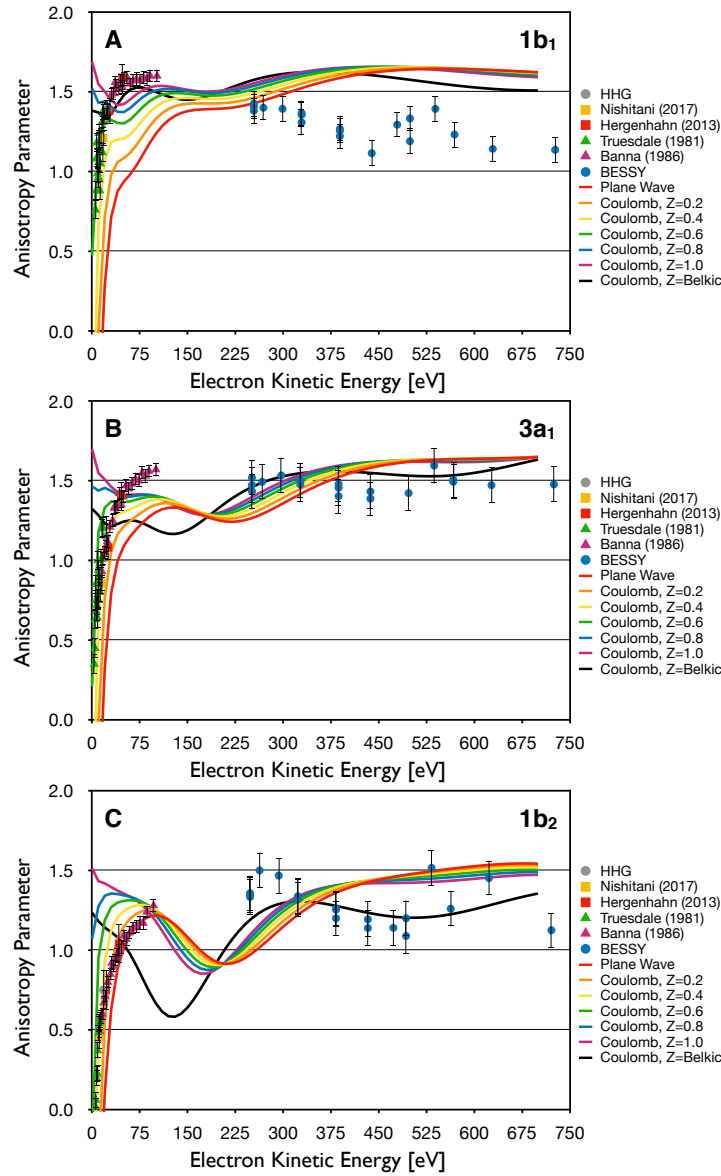


FIG. S8: β for water ionization computed with plane wave (red) and Coulomb waves with various charges (rainbow colors); the calculations with the Belkić's charges are shown in black. Single-center expansion placed on the oxygen atom; aug-cc-pVTZ.

After determining the center of expansion, we next look at the treatment of the electrostatic interaction between the photoelectron and the ionized core. Figure S8 shows anisotropies for the $1b_1$, $3a_1$, and $1b_2$ states of an isolated water molecule with different choices of Z_{eff} .

We note that the experimental points in the high-energy range are extracted from the microjet measurements rather than pure gas phase. Thus, these values can be affected by the deconvolution procedure and by the back-scattering from the jet. Out of the three bands, the results for $1b_1$ are probably most reliable due to a sharp and prominent peak in the measured spectrum (see Fig. S2). Neglecting the threshold regime (below 20 eV), we observe that:

- In the high-energy range (above 200 eV), all computed β 's follow the same trend (small amplitude oscillations for $1b_1$ and $3a_1$ and larger oscillations for $1b_2$);
- The spread of different theoretical values is about 10%;
- The largest deviation between theory and high-energy experiment is 30%;
- Theory, on average, slightly overestimates β at high energies;
- At high energies, the best agreement is obtained with Belkić's charges (mean absolute deviation in β of 0.28, 0.07, and 0.10 for $1b_1$, $3a_1$, and $1b_2$, respectively);
- At threshold, Coulomb waves with smaller charges can provide reasonable fit, which is consistent with the results for total cross sections[21].

B. Details of calculations for monomer, dimer, pentamer, and larger clusters

The β values of the monomer were obtained on structures optimized with ω B97X-D/aug-cc-pVTZ [33]. Dyson orbitals and ionization energies were computed with EOM-IP-CCSD/aug-cc-pVTZ [34–36].

To verify that the optimized monomer is a good model for gas phase water and that β is not sensitive to the geometry of the monomer, we performed an *ab initio* molecular dynamics (AIMD) simulation of a single gas-phase water molecule and computed the β from 100 different geometries. Specifically, we randomly sampled a set of 100 initial geometries

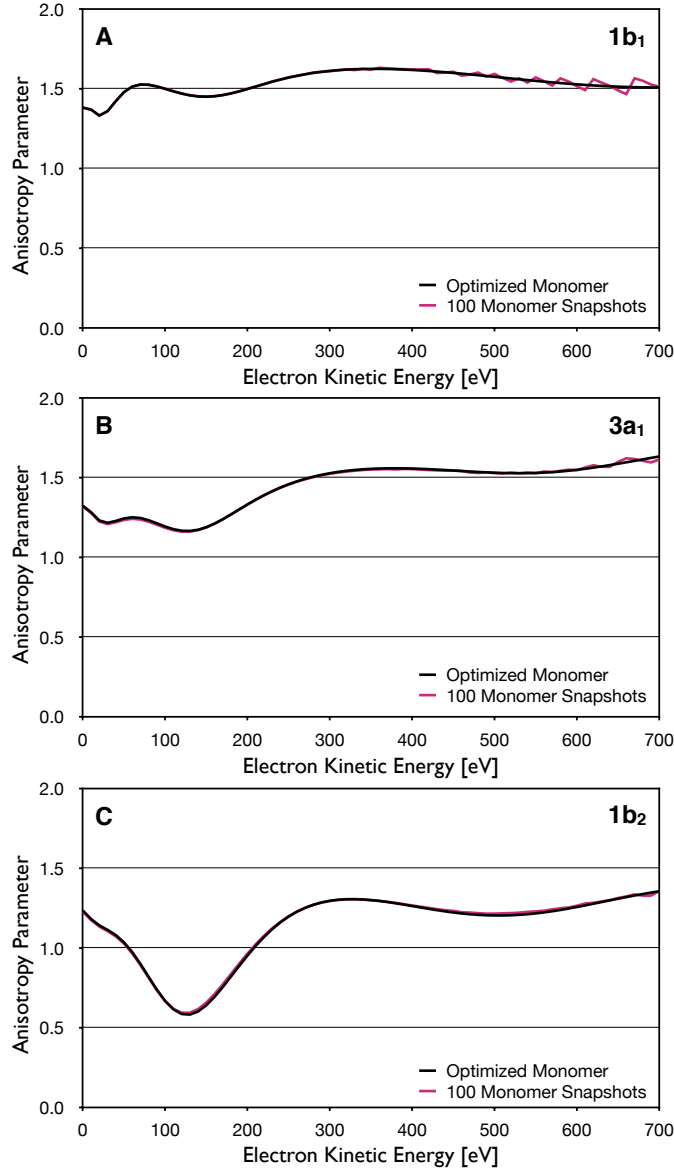


FIG. S9: β for water ionization computed for an optimized monomer (black) and as an average of 100 monomer snapshots (magenta) computed from an *ab initio* molecular dynamics (AIMD) simulation. Calculations in this figure employ the single-center expansion placed on the oxygen atom, a Coulomb wave treatment of the photoelectron with Belkić's charges, and Dyson orbitals computed with the aug-cc-pVTZ basis set.

and velocities from a Maxwell-Boltzmann distribution, propagated each trajectory for 100 fs (with a time-step of 1 fs) at the ω B97X-D/cc-pVTZ level of theory, and used the final structure to compute the Dyson orbital and corresponding β . The results show that for all three valence orbitals the dynamics have no effect on the β (see Fig. S9).

We carried out model dimer calculations as follows. A monomer was optimized and then

a dimer was produced by generating a copy of the monomer and translating it along the x axis. This results in a perfectly symmetric dimer structure where the water oxygen atoms are 6 Å apart. In the absence of interaction between the two water molecules, their degenerate orbitals can be expressed as any (normalized) linear combination of the two valence states of the monomers. The results of these calculations are shown in Fig. 3 of the main manuscript.

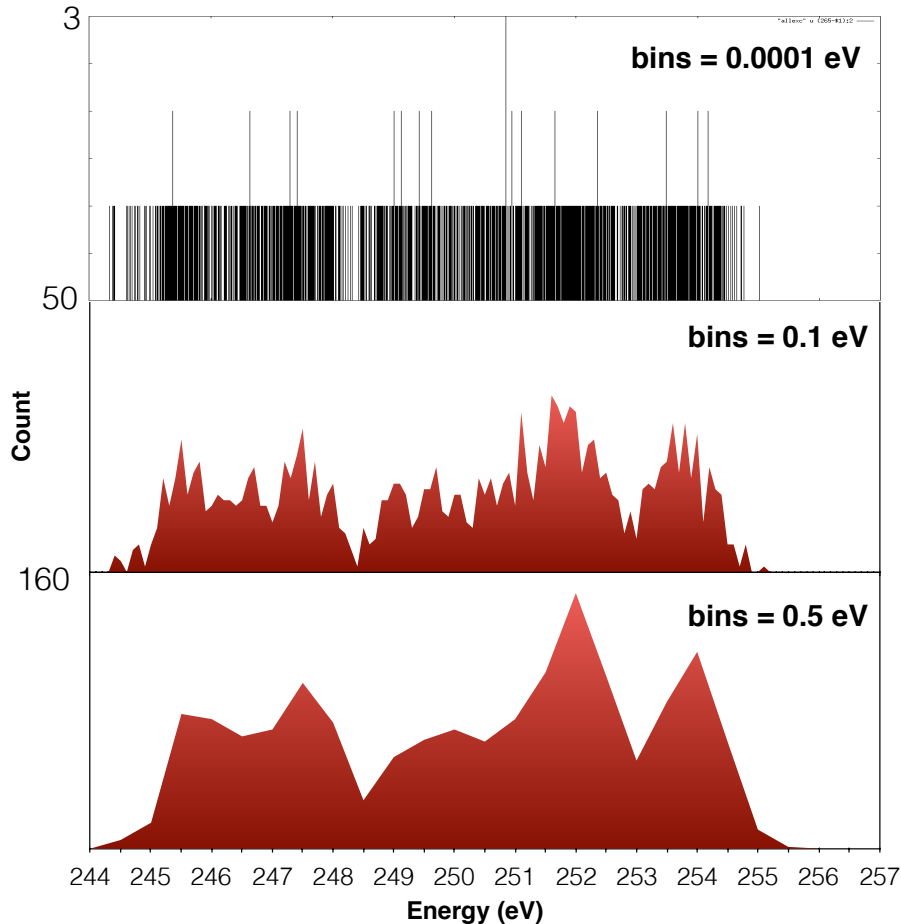


FIG. S10: Area plot of electronic kinetic energies from computed EOM-IP-CCSD ionization energies of all valence orbitals of 100 pentamer snapshots, assuming 265 eV photon energy. Three different bin sizes are shown. All three plots plot roughly indicate that there are five main peaks where EOM-IP energies are more concentrated.

The pentamer geometries were obtained from molecular dynamics simulations of liquid water with *Tinker* [37] using the TIP3P force field [38] in a periodic boundary box of $40\text{\AA} \times 40\text{\AA} \times 40\text{\AA}$. The system was equilibrated for 1 ns and followed by a production run of 500 ps, where a snapshot was taken every 5 ps, yielding 100 snapshots. From each snapshot, a pentamer was extracted by selecting a random water molecule far from the edge of the box and its four nearest neighbors. This procedure ensures that the pentamer snapshots

are uncorrelated. For each snapshot, ionization energies and Dyson orbitals were computed for the 15 valence states with EOM-IP-CCSD/aug-cc-pVDZ. The simulated photoelectron spectrum in Fig. 1A of the main manuscript is derived from the computed EOM-IP-CCSD ionization energies using an area plot showing the count of ionization energies within a certain range (we used a 0.5 eV bin size). More specifically, the figure is a histogram representing kinetic energies for electrons ionized from valence orbitals of 100 pentamer snapshots at 265 eV. The plot shows features of both liquid- and gas-phase peaks, and so is colored accordingly with the grey peak representing $1b_1(l)$, yellow representing a combination of $3a_1(l)$ and $1b_1(g)$, green representing $3a_1(g)$ and $1b_2(g)$, and red representing $1b_2(l)$. Notably, the simulated spectrum still shows the five main features, even if the area plot is plotted with different bin sizes (see Fig. S10).

Next, we look at the effect of the water cluster size on the β anisotropy, using the same multi-center model used for the pentamer. As shown in Fig. S11, larger clusters (hexamer and heptamer) show a negligible change in β relative to the pentamer.

C. Photoionization of the $1s_O$ core orbitals

To test the main assumption that scattering is responsible for reducing the β for the $1s_O$ core orbital in liquid[1, 39], we carried out calculations of the core-level Dyson orbitals of a water monomer and a randomly selected water pentamer. We used the core-valence separation variant of EOM-IP-CCSD, fc-CVS-EOM-IP-CCSD[40], and the aug-cc-pVTZ basis set. In the pentamer calculation, it was not necessary to enforce multi-core expansion since the five core $1s_O$ orbitals were all localized. The results are shown in Fig. S12. As expected, owing to the localized nature of the $1s_O$, it has nearly perfect s character, leading to $\beta=2$ at energies above 30 eV, although we note a small reduction of β at low energies (<20 eV). The experimentally[1] determined β rises much more slowly, reaching the limiting value of $\beta=2$ only at around 100 eV. This slow rise can be attributed to the scattering from hydrogens, which is neglected in our calculations. We note that calculations by Decleva and coworkers[41] do capture this behavior because they include the interaction of the outgoing electron with the core. Nevertheless, these results indicate that for $1s_O$ ionization, the scattering from the hydrogens becomes insignificant at energies considerably lower than one would expect from the de Broglie estimate (100 eV versus ~ 160 eV).

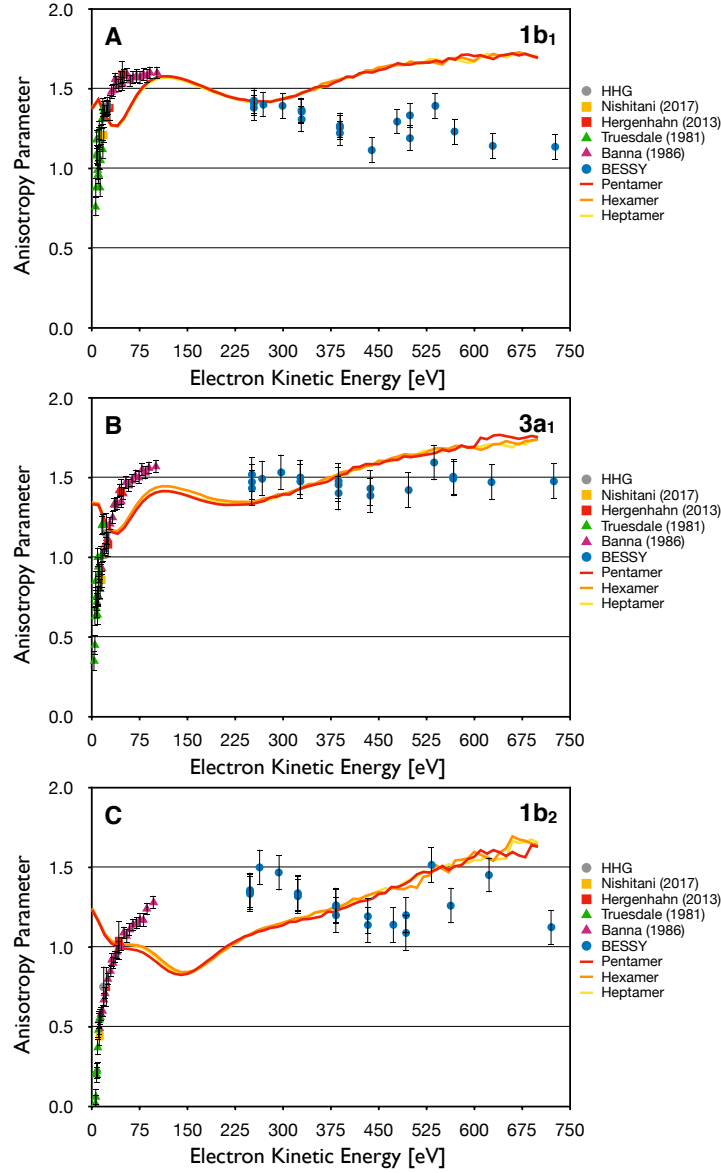


FIG. S11: β for water ionization computed for a pentamer (red), a hexamer (orange), and a heptamer (yellow) using the multi-center (localized) model with the center of expansion placed on the oxygen atom, a Coulomb wave treatment of the photoelectron with Belkić's charges, and Dyson orbitals computed with the aug-cc-pVDZ basis set. The results are averaged over valence states falling within the energy range of the corresponding band in Fig. 1 of the manuscript. Oscillations at high energy are due to numerical noise (small sampling size of states corresponding to a single structure).

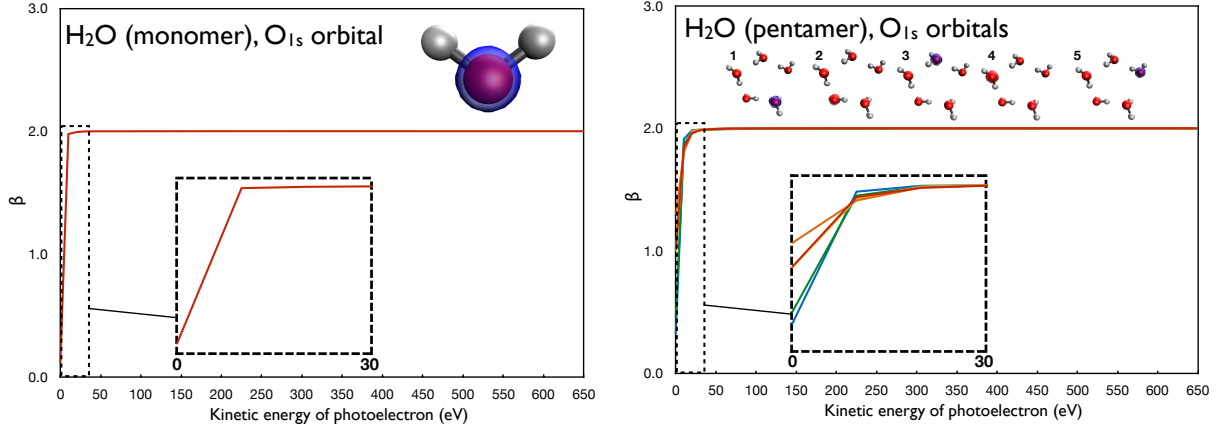


FIG. S12: Computed β values for the core $1s_O$ orbital as a function of energy for water molecule (left) and a water pentamer (right).

III. GAS-PHASE VERSUS LIQUID ANISOTROPIES: THEORY AND EXPERIMENT

To directly analyze the reduction of anisotropies in liquid relative to the gas-phase, we introduce the reduced β defined as:

$$\beta_{red} \equiv 1 - \frac{\beta_l}{\beta_g}, \quad (\text{S24})$$

where β_l and β_g denote liquid and gas-phase anisotropies. If the anisotropy in the liquid phase is the same as in the gas phase, then $\beta_{red} = 0$. Conversely, $\beta_{red} \approx 1$ signifies a complete loss of anisotropy in liquid. The results are collected in Fig. 7 of the main manuscript; here we provide an alternative representation.

Left panels of Fig. S13 show measured anisotropies (see Section I for the detailed explanation of the data analysis) for liquid and gas-phase water. Fig. S14 shows the theoretical values of the anisotropies and β_{red} for the isolated water molecule and for water pentamers. In the case of the pentamer, the approximate assignment of the ionized states to specific bands (e.g., $1b_1$, $3a_1$, $1b_2$) is carried out using energy criteria, as explained above. As one can see, β for pentamers are very close to those of the monomer, giving rise to $\beta_{red} \approx 0$. The arbitrariness with band assignments is responsible for slightly negative values of theoretical β_{red} for the $3a_1$ and $1b_2$ bands.

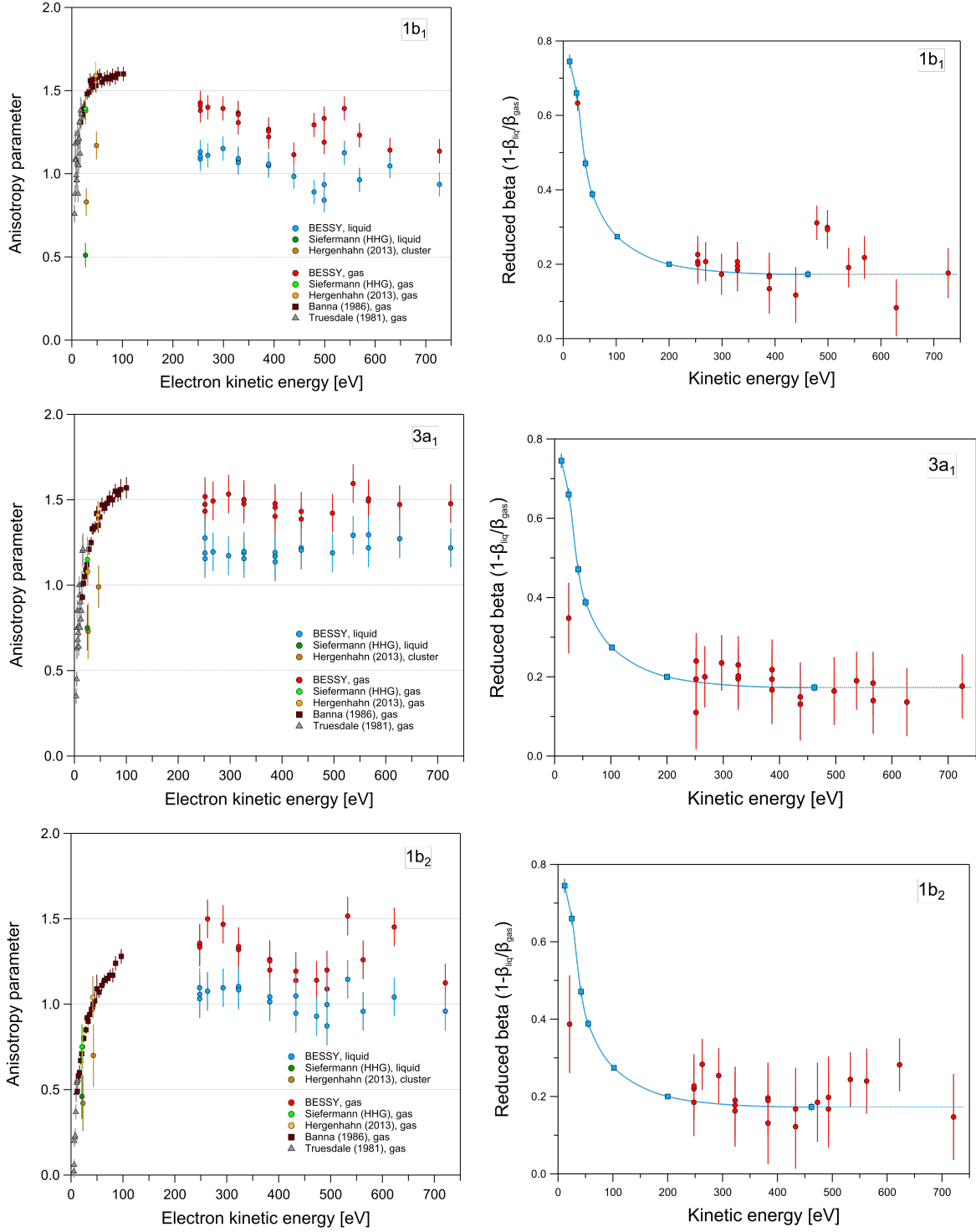


FIG. S13: Left: Liquid and gas-phase experimentally determined anisotropies. Right: the corresponding β_{red} . The solid blue line on the right shows β_{red} for $1s_O$.

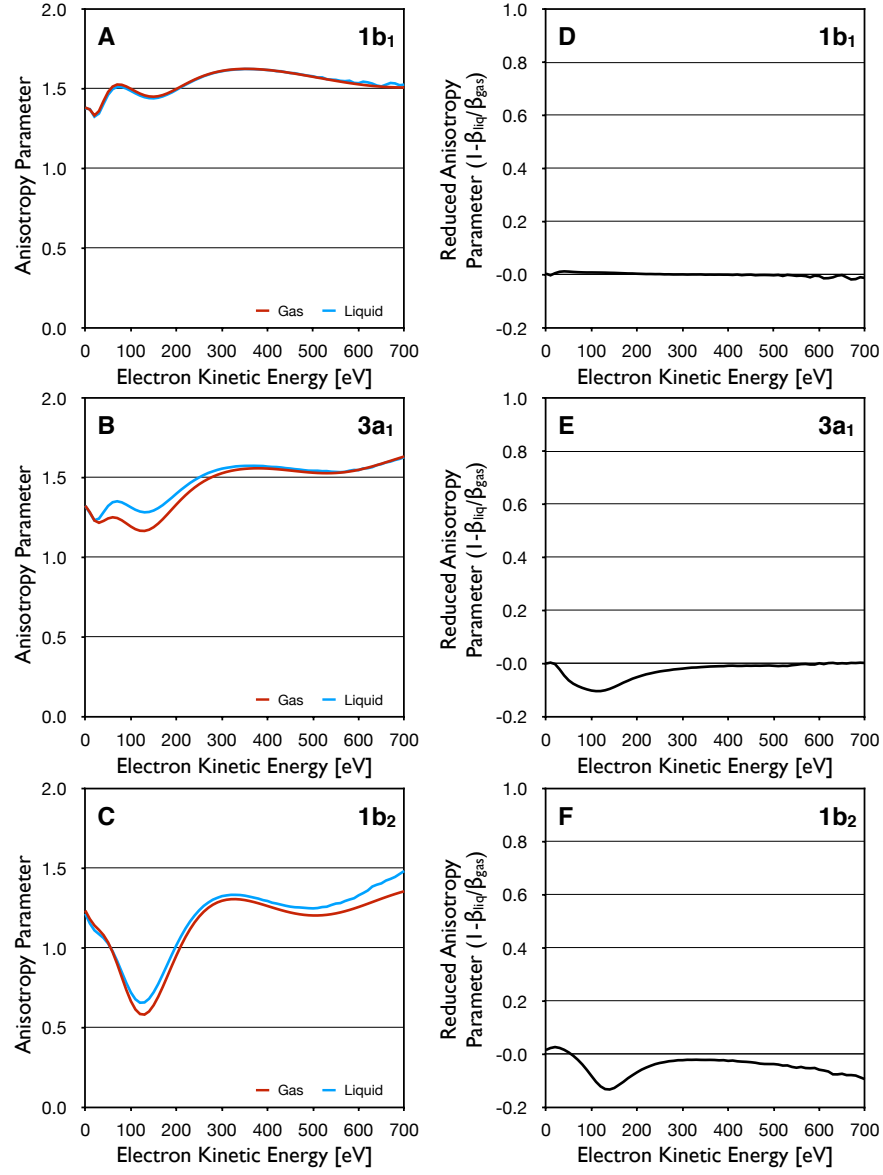


FIG. S14: Left: Theoretical values for liquid and gas-phase anisotropies. Right: Theoretical β_{red} .

IV. REFERENCES

- [1] Thürmer, S.; Seidel, R.; Faubel, M.; Eberhardt, W.; Hemminger, J. C.; Bradforth, S. E.; Winter, B. Photoelectron angular distributions from liquid water: Effects of electron scattering *Phys. Rev. Lett.* **2013**, *111*, 173005.
- [2] Jablonski, A. Angular distribution of photoelectrons emitted by the laboratory soft and hard X-ray radiation sources *J. Electron. Spectrosc. Relat. Phenom.* **2013**, *189*, 81–95.
- [3] Schmidt, V. *Electron Spectrometry of Atoms Using Synchrotron Radiation*, Cambridge Monographs on Atomic, Molecular and Chemical Physics; Cambridge University Press, 2005.
- [4] Derenbach, H.; Schmidt, V. Angular distribution of Kr $4s \rightarrow \epsilon p$ photoelectrons *J. Phys. B* **1984**, *17*, 83.
- [5] Seidel, R.; Pohl, M. N.; Ali, H.; Winter, B.; Aziz, E. F. Advances in liquid phase soft-x-ray photoemission spectroscopy: A new experimental setup at BESSY II *Rev. Sci. Instrum.* **2017**, *88*, 073107.
- [6] Sasaki, S. Analyses for a planar variably-polarizing undulator *Nuclear Instruments and Methods in Physics Research* **1994**, *347*, 83–86.
- [7] Bahrtdt, J.; Frentrup, W.; Gaupp, A.; Scheer, M.; Gudat, W.; Ingold, G.; Sasaki, S. Elliptically polarizing insertion devices at BESSY II *Nuclear Instruments and Methods in Physics Research* **2001**, *467-468*, 21 – 29; 7th Int.Conf. on Synchrotron Radiation Instrumentation.
- [8] Godehusen, K.; Mertins, H.-C.; Richter, T.; Zimmermann, P.; Martins, M. Electron-correlation effects in the angular distribution of photoelectrons from Kr investigated by rotating the polarization axis of undulator radiation *Phys. Rev. A* **2003**, *68*, 012711.
- [9] Winter, B.; Faubel, M. Photoemission from liquid aqueous solutions *Chem. Rev.* **2006**, *106*, 1176–1211.
- [10] Seidel, R.; Thürmer, S.; Winter, B. Photoelectron spectroscopy meets aqueous solution: Studies from a vacuum liquid microjet *J. Phys. Chem. Lett.* **2011**, *2*, 633–641.
- [11] Shirley, D. A. High-resolution X-ray photoemission spectrum of the valence bands of gold *Phys. Rev. B* **1972**, *5*, 4709–4714.
- [12] Proctor, A.; Sherwood, P. M. A. Data analysis techniques in x-ray photoelectron spectroscopy *Anal. Chem.* **1982**, *54*, 13–19.
- [13] Sherwood, P. M. A. In *Practical Surface Analysis by Auger and X-ray Photoelectron Spectroscopy*; D. Briggs, M. P. Seah, Ed.; Wiley: Chichester, 1983.
- [14] Winter, B.; Weber, R.; Widdra, W.; Dittmar, M.; Faubel, M.; Hertel, I. V. Full valence band photoemission from liquid water using EUV synchrotron radiation *J. Phys. Chem. A* **2004**, *108*, 2625–2631.
- [15] Faubel, M.; Siefermann, K. R.; Liu, Y.; Abel, B. Ultrafast soft X-ray photoelectron spectroscopy at liquid water microjets *Acc. Chem. Res.* **2012**, *45*, 120–130.
- [16] Schäfers, F. In *Modern Developments in X-Ray and Neutron Optics*; Erko, A., Idir, M., Krist, T., Michette, A. G., Eds.; Springer Berlin Heidelberg: Berlin, Heidelberg, 2008; p. 9.
- [17] Banna, M. S.; McQuaide, B. H.; Malutzki, R.; Schmidt, V. The photoelectron spectrum of water in the 30 to 140 eV photon energy range *J. Chem. Phys.* **1986**, *84*.
- [18] Zhang, C.; Andersson, T.; Förstel, M.; Mucke, M.; Arion, T.; Tchapyguine, M.; Björneholm, O.; Hergenroth, U. The photoelectron angular distribution of water clusters *J. Chem. Phys.*

- 2013**, 138, 234306.
- [19] Shao, Y.; Gan, Z.; Epifanovsky, E.; Gilbert, A.T.B.; Wormit, M.; Kussmann, J.; Lange, A.W.; Behn, A.; Deng, J.; Feng, X., et al. Advances in molecular quantum chemistry contained in the Q-Chem 4 program package *Mol. Phys.* **2015**, 113, 184–215.
 - [20] ezDyson user’s manual. Gozem, S.; Krylov, A. I. **2015**;
ezDyson, <http://iopenshell.usc.edu/downloads/>.
 - [21] Gozem, S.; Gunina, A. O.; Ichino, T.; Osborn, D. L.; Stanton, J. F.; Krylov, A. I. Photoelectron wave function in photoionization: Plane wave or Coulomb wave? *J. Phys. Chem. Lett.* **2015**, 6, 4532–4540.
 - [22] Oana, C. M.; Krylov, A. I. Dyson orbitals for ionization from the ground and electronically excited states within equation-of-motion coupled-cluster formalism: Theory, implementation, and examples *J. Chem. Phys.* **2007**, 127, 234106–14.
 - [23] Oana, C. M.; Krylov, A. I. Cross sections and photoelectron angular distributions in photodetachment from negative ions using equation-of-motion coupled-cluster Dyson orbitals *J. Chem. Phys.* **2009**, 131, 124114–15.
 - [24] Krylov, A. I. Equation-of-motion coupled-cluster methods for open-shell and electronically excited species: The hitchhiker’s guide to Fock space *Annu. Rev. Phys. Chem.* **2008**, 59, 433–462.
 - [25] Sakurai, J. J. *Modern Quantum Mechanics*; Addison-Wesley Publishing Company, 1995.
 - [26] Lin, Y.; Ning, C. Calculation of photodetachment cross sections and photoelectron angular distributions of negative ions using density functional theory *J. Chem. Phys.* **2015**, 143, 144310.
 - [27] Martini, L.; Boll, D. I. R.; Fojón, O. A. Interferences in the photoionization of water molecules *J. Phys. B* **2019**, 52, 105204.
 - [28] Belkić, D. V. z.; Gayet, R.; Salin, A. Electron capture in high-energy ion-atom collisions *Phys. Rep.* **1979**, 56, 279.
 - [29] Slater, J. C. Atomic shielding constants *Phys. Rev.* **1930**, 36, 57.
 - [30] Ciappina, M. F.; Fojón, O. A.; Rivarola, R. D. Coherent electron emission from simple molecules by impact of energetic charged particles *J. Phys. B* **2014**, 47, 042001.
 - [31] Mabbs, R.; Pichugin, K.; Sanov, A. Dynamic molecular interferometer: probe of inversion symmetry in I_2^- photodissociation *J. Chem. Phys.* **2005**, 123, 054329.
 - [32] Clark, G. N. I.; Cappa, C. D.; Smith, J. D.; Saykally, R. J.; Head-Gordon, T. The structure of ambient water *Mol. Phys.* **2010**, 108, 1415–1433.
 - [33] Chai, J.-D.; Head-Gordon, M. Long-range corrected hybrid density functionals with damped atom-atom dispersion interactions *Phys. Chem. Chem. Phys.* **2008**, 10, 6615–6620.
 - [34] Stanton, J. F.; Gauss, J. Analytic energy derivatives for ionized states described by the equation-of-motion coupled cluster method *J. Chem. Phys.* **1994**, 101, 8938–8944.
 - [35] Stanton, J. F.; Gauss, J. A simple scheme for the direct calculation of ionization potentials with coupled-cluster theory that exploits established excitation energy methods *J. Chem. Phys.* **1999**, 111, 8785–8788.
 - [36] Pieniazek, P. A.; Arnstein, S. A.; Bradforth, S. E.; Krylov, A. I.; Sherrill, C. D. Benchmark full configuration interaction and EOM-IP-CCSD results for prototypical charge transfer systems: Noncovalent ionized dimers *J. Chem. Phys.* **2007**, 127, 164110.
 - [37] Ponder, J.W. TINKER – Software Tools for Molecular Design, URL <http://dasher.wustl.edu/tinker/> (accessed on April 23, 2017).
 - [38] Jorgensen, William L.; Chandrasekhar, Jayaraman; Madura, Jeffry D.; Impey, Roger W.;

- Klein, Michael L. Comparison of simple potential functions for simulating liquid water *The Journal of Chemical Physics* **1983**, *79*, 926–935.
- [39] Ottosson, N.; Faubel, M.; Bradforth, S. E.; Jungwirth, P.; Winter, B. Photoelectron spectroscopy of liquid water and aqueous solution: Electron effective attenuation lengths and emission-angle anisotropy *J. Electron Spectrosc. Relat. Phenom.* **2010**, *177*, 60–70.
- [40] Vidal, M. L.; Feng, X.; Epifanovski, E.; Krylov, A. I.; Coriani, S. A new and efficient equation-of-motion coupled-cluster framework for core-excited and core-ionized states *J. Chem. Theory Comput.* **2019**, *15*, 3117–3133.
- [41] Stener, M.; Fronzoni, G.; Toffoli, D.; Decleva, P. Time dependent density functional photoionization of CH₄, NH₃, H₂O and HF *Chem. Phys. Lett.* **2002**, *282*, 337–351.
- [42] We note that the minimum in the $F(\omega)$ function, defined as a ratio of the full cross-section to the atomic contributions, shown in Figs. 4 and 6 in Ref. [27] happens at about 160 eV. Also, the integral is zero for half-period, i.e., when $E = \frac{1}{2} \left(\frac{\pi}{R_{AB}} \right)^2$, that is, at 41 eV, which is close to the energy where $F(\omega)$ pass through the maximum.